

# Using the polarization properties of double radio relics to probe the turbulent compression scenario

C. Stuardi<sup>1,2</sup>, A. Bonafede<sup>1,2</sup>, K. Rajpurohit<sup>1,2</sup>, M. Brüggen<sup>3</sup>, F. de Gasperin<sup>2</sup>, D. Hoang<sup>3</sup>, R. J. van Weeren<sup>4</sup> and F. Vazza<sup>1,2,3</sup>

<sup>1</sup> Dipartimento di Fisica e Astronomia, Università di Bologna, via Gobetti 93/2, I-40129 Bologna, Italy  
e-mail: chiara.stuardi2@unibo.it

<sup>2</sup> INAF - Istituto di Radioastronomia di Bologna, Via Gobetti 101, I-40129 Bologna, Italy

<sup>3</sup> Hamburger Sternwarte, Universität Hamburg, Gojenbergsweg 112, 21029 Hamburg, Germany

<sup>4</sup> Leiden Observatory, Leiden University, PO Box 9513, 2300 RA Leiden, The Netherlands

Received XX; accepted YY

## ABSTRACT

**Context.** Radio relics are Mpc-size synchrotron sources located in the outskirts of some merging galaxy clusters. Binary-merging systems with favorable orientation may host two almost symmetric relics, named double radio relics.

**Aims.** Double radio relics are seen preferentially edge-on and, thus, constitute a privileged sample for statistical studies. Their polarization and Faraday rotation properties give direct access to the relics' origin and magnetic fields.

**Methods.** In this paper, we present a polarization and Rotation Measure (RM) synthesis study of four clusters hosting double radio relics, namely 8C 0212+703, Abell 3365, PLCK G287.0+32.9, previously missing polarization studies, and ZwCl 2341+0000, for which conflicting results have been reported. We used 1-2 GHz Karl G. Jansky Very Large Array observations. We also provide an updated compilation of known double radio relics with important observed quantities. We studied their polarization and Faraday rotation properties at 1.4 GHz and we searched for correlations between fractional polarization and physical resolution, distance from the cluster center, and shock Mach number.

**Results.** The weak correlations found between these quantities are well reproduced by state-of-the-art magneto-hydrodynamical simulations of radio relics, confirming that merger shock waves propagate in a turbulent medium with tangled magnetic fields. Both external and internal Faraday depolarization should play a fundamental role in determining the polarization properties of radio relics at 1.4 GHz. Although the number of double radio relics with RM information is still low, their Faraday rotation properties (i.e., rest-frame RM and RM dispersion below 40 rad m<sup>-2</sup> and non-Gaussian RM distribution) can be explained in the scenario in which shock waves with Mach numbers larger than 2.5 propagate along the plane of the sky and compress the turbulent intra-cluster medium.

**Key words.** galaxies: clusters: individual: 8C 0212+703 – galaxies: clusters: individual: Abell 3365 – galaxies: clusters: individual: PLCK G287.0+32.9 – galaxies: clusters: individual: ZwCl 2341+0000 – galaxies: clusters: intracluster medium – magnetic fields

## 1. Introduction

A large variety of diffuse synchrotron sources populates galaxy clusters. They unveil the non-thermal content of the intra-cluster medium (ICM): weak magnetic fields ( $\sim 10 - 0.1 \mu\text{G}$ ) and relativistic particles. In particular, radio relics are observed in some galaxy clusters that have recently experienced a major merger as a consequence of hierarchical accretion processes (see e.g., van Weeren et al. 2019, for a recent review).

Radio relics are Mpc-size synchrotron sources observed in the outskirts of a few galaxy clusters. They often show an arc-like shape, with the curvature pointing towards the cluster center, and high levels of fractional polarization (i.e.,  $> 20\%$  at GHz frequencies). Their spectrum (defined by the flux density  $S_\nu \propto \nu^{-\alpha}$ ) is steep, with  $\alpha > 1$ , and often characterized by a steepening trend towards the cluster center. Double radio relics are a particular class of relics where two almost symmetric relics are observed on the opposite sides of the cluster center, along the main merger axis (see e.g., Bonafede et al. 2009; de Gasperin et al. 2014; Bonafede et al. 2017).

It is well established that the origin of radio relics is connected with the presence of shocks injected in the ICM during the merger event (Ensslin et al. 1998). Proof of this is the de-

tection of surface brightness and/or temperature jumps in the X-ray observations of the majority of radio relics with suitable X-ray data (e.g., Akamatsu & Kawahara 2013) and, *vice versa*, the detection of radio relics coincident with every X-ray detected cluster's shock (see Hlavacek-Larrondo et al. 2018, for a recent detection). The emerging scenario is that shock waves are able to both accelerate the electrons responsible for the synchrotron emission, via Fermi I processes, and compress and amplify the magnetic field components along the shock plane (Ensslin et al. 1998; Hoeft & Brüggen 2007).

In this framework, it is expected that an idealized binary merger can generate two merger shock waves that travel into the opposite directions along the merger axis forming double radio relics (Roettiger et al. 1999; Ha et al. 2018). A recent and comprehensive optical study confirmed that the merger axis of double relic galaxy clusters is preferentially near to the plane of the sky (Golovich et al. 2019a,b). Hence, double radio relics systems form an important sample because their merger geometry can be well constrained and projection effects on radio relics should be minimal since they are observed edge-on.

However, in this picture, a number of details are still missing. The major open question concerns the efficiency of the Diffusive

Shock Acceleration (DSA) process which is invoked to accelerate particles from the thermal pool (Jones & Ellison 1991). The predicted efficiency is not sufficient to produce the observed radio power considering the low Mach numbers ( $M < 5$ ) measured from radio relics (e.g., Botteon et al. 2020). For this problem, there are two broad classes of solutions: one is the presence of mildly relativistic fossil electrons in the ICM, which provide the seeds for successive re-acceleration via DSA (Pinzke et al. 2013; Kang & Ryu 2016; Inchingolo et al. 2022), the other involves processes of pre-acceleration of thermal electrons at the shock front (Guo et al. 2014a,b; Wittor et al. 2020). None of the two is actually validated to solve the efficiency problem. Other issues are the non-detection of  $\gamma$ -ray emission from galaxy clusters which would be also expected in case of DSA (Vazza & Brüggen 2014; Vazza et al. 2016), and the radio spectral index of some relics that is incompatible with the DSA theory. The latter is the case of  $\alpha < 1$  (see e.g., the southern relic in Abell 3667, de Gasperin et al. 2022) and curved spectral index (as observed in the fainter relics of the Toothbrush galaxy cluster, Rajpurohit et al. 2020).

Moreover, the role of magnetic fields in shaping radio relic emission is yet poorly understood. For example, it is questionable whether threads and filaments with an enhanced magnetic field strength could give origin to the filamentary structures observed in highly resolved images of radio relics (Di Gennaro et al. 2018; Rajpurohit et al. 2022b; de Gasperin et al. 2022). It is uncertain if magnetic fields can play an important role in particle acceleration since, for some mechanisms, the acceleration efficiency has a strong dependence on the pre-shock magnetic field alignment (i.e., Guo et al. 2014a; Caprioli & Spitkovsky 2014). While it is known that intra-cluster magnetic fields can be amplified by a factor  $\sim 2$  by compression for  $M \sim 2 - 3$  shocks (Iapichino & Brüggen 2012; Domínguez-Fernández et al. 2021), the numerous mechanisms that could lead to amplification in the low Mach number regime are still little explored from a theoretical point of view (Donnert et al. 2018). Also, a quantitative estimate of magnetic field amplification at relics is difficult to obtain and the number of studies is limited (Johnston-Hollitt & Ekers 2004; Bonafede et al. 2013; Stuardi et al. 2021).

A powerful tool to study magnetic fields in cluster radio relics is the analysis of their polarized emission. Since magnetic fields in relics are compressed and ordered along the shock plane, they are expected to be intrinsically highly polarized (Ensslin et al. 1998). Their polarized emission carries fundamental information about their origin. In particular, their polarization properties (as the average fractional polarization and the spatial distribution of the fractional polarization across the relic) are strictly connected to the ICM turbulent properties and magnetic field structure (Wittor et al. 2019; Domínguez-Fernández et al. 2021). The direction of intrinsic polarization angle unveils the direction of the source magnetic field projected on the plane of the sky ( $B_{\perp}$ ), while the rotation of the polarization angle with frequency, i.e. the Faraday rotation effect, depends on the magnetic field component of the magnetic field along the line-of-sight ( $B_{\parallel}$ ) through the Rotation Measure (RM).

Following (Burn 1966) we can express the polarization as a complex vector:

$$\mathbf{P} = Q + iU = Pe^{i\chi}, \quad (1)$$

where  $\chi$  is the polarization angle and  $Q$  and  $U$  are the Stokes parameters. The measured polarization angle depends on the observing wavelength squared,  $\lambda^2$ , and on the Faraday depth,  $\phi$ :

$$\chi(\lambda^2) = \chi_0 + \phi\lambda^2, \quad (2)$$

where  $\chi_0$  is the intrinsic polarization angle of the radiation and the Faraday depth is defined as:

$$\phi = 0.81 \int_{\text{source}}^{\text{observer}} n_e B_{\parallel} dl \text{ [rad m}^{-2}\text{]} \quad (3)$$

with  $n_e$ , the thermal electron density, in  $\text{cm}^{-3}$ ,  $B_{\parallel}$  in  $\mu\text{G}$  and  $dl$ , the infinitesimal path length, in parsecs. The Rotation Measure is :

$$RM = \frac{d\chi(\lambda^2)}{d\lambda^2} \quad (4)$$

and  $RM = \phi$  only when  $\chi$  and  $\lambda^2$  are linearly correlated, i.e. when the Faraday rotation is caused by one or more (not emitting) screens in the source's foreground. This is often the case for radio relics, for which the measured RM is the sum of the Milky Way Faraday rotation and of the contribution from the external ICM. For this reason, RMs from relics can be used to define the relics position within the ICM and to infer the properties of the magnetic field in front of the relics themselves (Pizzo et al. 2011; Stuardi et al. 2021; Rajpurohit et al. 2022a). When more complex Faraday depth structures are observed from radio relics, they are an indication of internal Faraday rotation and can be used to study the internal magneto-ionic structure of radio relics (Stuardi et al. 2019; Rajpurohit et al. 2022a; de Gasperin et al. 2022). Faraday effects may also cause wavelength-dependent depolarization (Burn 1966). Hence, the depolarization observed from relics is another important probe of magnetic field structure.

Polarization and, in particular, Faraday rotation studies of radio relics are still scarce in the literature. Only few bright radio relics have been studied in polarization with a good frequency coverage and physical resolution below 25 kpc (Owen et al. 2014; Di Gennaro et al. 2021; Rajpurohit et al. 2022a; de Gasperin et al. 2022). For most radio relics we only have information on their fractional polarization. This is true also for double radio relics, despite these systems may constitute a privileged sample because their geometry should favor the detection of their polarized emission (Wittor et al. 2019).

Making a census of all double radio relics, we realized that three well-known radio relics totally miss radio polarization observations available in the literature, namely 8C 0212+703 (a.k.a. CIG 0217+70), Abell 3365 and PLCK G287.0+32.9 (a.k.a. PSZ2 G286.98+32.90). Hence, here we provide polarization and Faraday rotation images for these three galaxy clusters performed with 1 – 2 GHz Karl G. Jansky Very Large Array (JVLA) observations. We decided also to analyze 1 – 2 GHz JVLA observations of the double relic galaxy cluster ZwCl 2341.1+0000, for which polarization studies are already available but only at higher frequencies (Benson et al. 2017) or at low-resolution (Giovannini et al. 2010). The main properties of the four clusters analyzed in this paper are listed in Tab. 1.

With this work, we want (i) to increase the number of double radio relics with available polarization and Faraday rotation information and (ii) to provide an insight into the polarization

**Table 1.** Double relic galaxy clusters analyzed in this work. Column 1: name of the cluster; Column 2 and 3: J2000 celestial coordinates retrieved from the NASA/IPAC Extragalactic Database (NED, <https://ned.ipac.caltech.edu/>); Column 4: redshift,  $z$ , retrieved from NED with the exception of 8C 0212+703 for which an updated redshift is provided by Zhang et al. (2020); Column 5: Galactic Faraday rotation computed as the median of the Milky Way RM from Hutschenreuter et al. (2021) in a 1 degree diameter circle around the cluster position. The uncertainty is the average uncertainty within this circle.

Cluster	R.A.	Dec	$z$	Galactic RM
8C 0212+703	02 <sup>h</sup> 17 <sup>m</sup> 01 <sup>s</sup>	+70°36′.3	0.180	$-24 \pm 21 \text{ rad m}^{-2}$
Abell 3365	05 <sup>h</sup> 48 <sup>m</sup> 13 <sup>s</sup>	-21°56′.1	0.093	$26 \pm 10 \text{ rad m}^{-2}$
PLCK G287.0+32.9	11 <sup>h</sup> 50 <sup>m</sup> 49 <sup>s</sup>	-28°04′.6	0.390	$-34 \pm 12 \text{ rad m}^{-2}$
ZwCl 2341.1+0000	23 <sup>h</sup> 43 <sup>m</sup> 39 <sup>s</sup>	+00°16′.7	0.270	$-8 \pm 7 \text{ rad m}^{-2}$

properties of all double radio relics known to date in order to probe their origin.

This paper is organized as follows: this introductory section is completed with a brief overview on available information for the four double relic galaxy clusters here analyzed; in Sec. 2 we present our radio observations and the polarization analysis; in Sec. 3 we present our results; in Sec 4 we discuss our results in comparison with magneto-hydrodynamical (MHD) simulations of radio relics and with an updated compilation of all double radio relics, while in Sec. 5 we summarize and draw the conclusion of our work. The broadband integrated radio spectra of a few double radio relics is computed in the Appendix A.

Throughout this paper, we assume a  $\Lambda$ CDM cosmological model, with  $H_0 = 69.6 \text{ km s}^{-1} \text{ Mpc}^{-1}$ ,  $\Omega_M = 0.286$ ,  $\Omega_\Lambda = 0.714$  (Bennett et al. 2014).

### 1.1. 8C 0212+703 (CIG 0217+70)

The radio diffuse emission of the galaxy cluster 8C 0212+703, hereafter 8C0212, was first discovered in the Westerbork Northern Sky Survey (Rengelink et al. 1997, WENSS) by Delain & Rudnick (2006). Comparing radio, X-ray, and optical data, Brown & Rudnick (2011) confirmed the presence of a central radio halo and of multiple radio relics. A recent study based on the spectroscopy of X-ray *Chandra* data was able to revise the redshift of 8C0212 which is now established to be  $z = 0.18$  (Zhang et al. 2020). This made 8C0212 the galaxy cluster hosting the largest radio relic detected to date, with a projected linear size of 3.5 Mpc (Hoang et al. 2021).

The low-frequency radio emission of this cluster was studied by Hoang et al. (2021) using the Low Frequency Array (van Haarlem et al. 2013, LOFAR). Part of the data presented in this paper were also used by Hoang et al. (2021) to make spectral index maps between 141 MHz and 1.5 GHz. This study confirmed the spectral index trend expected for relics both in the elongated western relic and in the spiral-like eastern one. Hoang et al. (2021) found injection spectral indexes  $\alpha_{141\text{MHz}}^{1.5\text{GHz}} = 0.72 \pm 0.05$  (for the western relic) and  $\alpha_{141\text{MHz}}^{1.5\text{GHz}} = 1.14 \pm 0.07, 0.93 \pm 0.08, 0.97 \pm 0.16$  (for the three patches that compose the eastern relic) leading to shocks Mach number estimates ranging between 2.0 and 3.2. High-resolution radio images also found a possible connection between the emission of a radio galaxy and the diffuse radio emission nearby the eastern relic. No connection has been established between the radio halo emission and the X-ray detected discontinuities at the halo edges (Zhang et al. 2020).

Hoang et al. (2021) did not provide polarization images of the diffuse radio sources. The detection of polarized emission

would be a confirmation of the identification as radio relics. A detailed study of the X-ray emission at the position of the relics is also missing because the data used by Zhang et al. (2019) only cover the central part of the cluster.

### 1.2. Abell 3365

Abell 3365 ( $z=0.093$  Abell 1958; Struble & Rood 1999), hereafter A3365, is a complex merging system little studied in the radio band. The eastern elongated radio relic was first discovered in the NRAO VLA Sky Survey (NVSS, Condon et al. 1998) and then observed at 1.4 GHz with the Westerbork Synthesis Radio Telescope (WSRT) and VLA (van Weeren et al. 2011a). The latter study discovered a second radio relic in the north-west of the cluster whose identification was confirmed by the detection of an underlying shock front with  $M = 3.9 \pm 0.8$  in the X-ray XMM-Newton images (Urdampilleta et al. 2021). Urdampilleta et al. (2021) discovered a second shock with  $M = 3.5 \pm 0.6$  at the position of the eastern relic and a cold front at the western edge of the highly disturbed and NE-SW elongated cluster core. Optical galaxies are distributed in three main structures (van Weeren et al. 2011a; Golovich et al. 2019a,b): the most massive first component in the north-east has itself two merging sub-components which may have originated the eastern relic, the second western sub-component is going to merge with the third one that lies in the middle. Recently, A3365 was observed with the Murchison Widefield Array (MWA) and the Australian Square Kilometre Array Pathfinder (ASKAP) by Duchesne et al. (2021a) which were able to constrain the integrated spectral index of the eastern and western relics ( $\alpha_{88\text{MHz}}^{1.4\text{GHz}} = 0.85 \pm 0.03$  and  $\alpha_{118\text{MHz}}^{1.4\text{GHz}} = 0.76 \pm 0.08$ , respectively). These estimates are incompatible with DSA theory.

### 1.3. PLCK G287.0+32.9 (PSZ2 G286.98+32.90)

PLCK G287.0+32.9, hereafter PLCK287, is an exceptionally luminous galaxy cluster at  $z = 0.39$  detected by the Planck satellite (Planck Collaboration et al. 2016). A pair of radio relics and a central radio halo were discovered by means of Giant Metrewave Radio Telescope (GMRT, at 150 MHz) and Very Large Array (1.4 GHz) observations by Bagchi et al. (2011). Bonafede et al. (2014) performed a detailed multi-wavelength analysis of this cluster. New GMRT (at 325 and 610 MHz) and JVLA (2-4 GHz) radio images were used to study the radio spectral index of the two radio relics. Spectral index estimates were used to derive the Mach number of the two relics:  $M \sim 3.7$  for the southern relic and  $M \sim 5.4$  for the northern one. The northern relic revealed a connection with the emission of a radio galaxy and a peculiar spectral index profile that steepens along both the internal and external side of the relic. George et al. (2017) also measured the integrated spectral index of the northern and southern relics obtaining  $\alpha_{88\text{MHz}}^{3\text{GHz}} = 1.19 \pm 0.03$  and  $\alpha_{88\text{MHz}}^{3\text{GHz}} = 1.36 \pm 0.04$ , respectively.

PLCK287 is undergoing a major merger along the NW-SE direction, slightly misaligned with respect to the optically detected intergalactic filament where the cluster is located (Bonafede et al. 2014). The different distances of the northern (400 kpc) and southern (2.8 Mpc) relic from the cluster center was used to infer a possible merging scenario where the southern relic was created by the first core passage towards the south while the northern relic originated in a second core-passage. Both the dynamical analysis of this cluster based on the optical spectroscopy (Golovich et al. 2019b) and the weak lensing anal-

ysis (Finner et al. 2017) found a weak signature of one (or multiple) sub-clusters nearby the southern radio relic. These components are not observed in the 10 ks XMM-Newton observation presented in Bagchi et al. (2011). Overall, the dynamics of the merger is not clear, in particular concerning the origin of the southern bright radio relic.

#### 1.4. ZwCl 2341.1+0000

ZwCl 2341.1+000, hereafter ZwCl2341, is the second most massive galaxy cluster of the Saraswati supercluster (Bagchi et al. 2017). It is located at  $z = 0.270$  (Golovich et al. 2019b) along a filament of galaxies at  $\sim 45$  Mpc from the supercluster core. Bagchi et al. (2002) first discovered the diffuse radio emission of this galaxy cluster using NVSS observations. They found that the radio emission likely originated from the formation process of a NW-SE elongated structure with a total extent of  $\sim 6$  Mpc that was also detected in the optical and X-ray observations. A detailed radio follow-up of this system was performed by van Weeren et al. (2009) using GMRT 610, 241, and 157 MHz images. They classified the northern and southern emissions as radio relics, although with a rather round shape. A tentative detection of a central extended emission connecting the radio relics was also reported at 1.4 GHz, first by Giovannini et al. (2010), using VLA observations, and more recently by Parekh et al. (2022) with the MeerKAT radio telescope (Jonas & MeerKAT Team 2016).

Giovannini et al. (2010) also reported polarized emission from the whole region of extended radio emission but, due to the very low-resolution ( $83'' \times 75''$ ), the emission of the relics could be blended with other cluster sources and subject to beam depolarization. They obtained a 15 % average polarization fraction for the northern relic and 8 % for the southern one at 1.4 GHz. Benson et al. (2017) published polarization images of ZwCl2341 using JVLA 2-4 GHz observations and obtained much lower average polarization fractions: 5 % for the northern relic and 8 % for the southern one which also shows a maximum polarization fraction of 30 %. Since higher fractional polarization is expected at higher frequencies, due to wavelength-dependent depolarization effects, a polarization study at 1.4 GHz at higher resolution is needed in order to investigate the discrepancy between these two results.

Several optical studies of this system (Boschin et al. 2013; Benson et al. 2017; Golovich et al. 2019b) found that it is composed of at least three sub-clusters: two of them are aligned along the NW-SE elongation of the X-ray emission and their merger is possibly responsible for the radio relics formation, while the third one in the north-east is likely to be involved in a secondary merger along the line-of-sight. Zhang et al. (2021) performed a detailed analysis of a deep 206.5 ks *Chandra* observation of ZwCl2341. They discovered the presence of numerous substructures within this cluster and confirmed its complex dynamical state. They could not detect shocks underlying the radio relics (as previously attempted by Akamatsu & Kawahara 2013; Ogrea et al. 2014) but they found a surface brightness edge at the position of the southern relic, which they interpreted as a kink due to the disrupted core of the southern sub-cluster. The northern relic lies instead at the apex of a conic X-ray structure delimited by cold fronts on both sides. Zhang et al. (2021) also presented resolved spectral index maps between 325 MHz GMRT and 1.5 GHz JVLA observations (the same that are used in this work). Both relics show a spectral steeping towards the center of the cluster although the trend is not very clear, also due to the patchy shape of the two relics. From the injection spectral index they es-

timated a radio Mach number  $M = 2.2 \pm 0.1$  and  $M = 2.4 \pm 0.4$  for the southern and northern relic, respectively.

## 2. Radio observations

The four clusters have been observed with the JVLA in the L-band (1 – 2 GHz) within the observing proposal 17A-083. In the case of ZwCl2341, we also analyzed two archival observations collected under the observing proposal SG0365. We used C- and D-configuration observations. 8C0212 and Abell 3365 were observed with two separated pointings on the two relics to maximize the sensitivity in the region of interest. The pointing center of each observation, the array configuration, and the observing date and time are summarized in Tab. 2. The L-band spans 1024 MHz, covered by 16 spectral windows of 64 MHz (and 64 1-MHz-channels) each. Full polarization products have been recorded.

### 2.1. Data reduction

The dataset were automatically pre-processed right after the observation with the VLA CASA<sup>1</sup> calibration pipeline (version 4.7.1 for D-array and 4.7.2 for C-array observations). This pipeline is optimized for Stokes I continuum data and it performs standard flagging and calibration procedures. We used the CASA 5.6.1 package to complete the calibration also for the cross-correlation polarization products and to perform additional flagging.

We used the Perley & Butler (2013) flux density scale for wide-band observations as a model for the primary calibrator of each observation. To build a frequency-dependent polarization model we made a polynomial fit to the values of linear polarization fraction and polarization angle of a polarized calibrator, following the NRAO polarimetry guide for polarization calibration<sup>2</sup>. An unpolarized source was used to calibrate the on-axis instrumental leakage. The final calibration tables were applied to the target.

Radio frequency interference (RFI) was removed manually and using statistical flagging algorithms also from the cross-correlation products. Some spectral windows were entirely removed. In particular spectral windows 1, 2, 3, 8, and 9 were often severely affected by RFI. The calibrated data were then averaged in time down to 10 s and in frequency with channels of 4 MHz, in order to speed up the subsequent imaging and self-calibration processes. We computed new visibility weights according to the visibilities scatter.

We used the multi-scale multi-frequency de-convolution algorithm of the CASA task *tclean* (Rau & Cornwell 2011) for wide-band synthesis-imaging. As a first step, we made a large image of the entire field of view ( $\sim 1^\circ \times 1^\circ$ ). We used a three Taylor expansion (*nterms* = 3) in order to take into account both the source spectral index and the primary beam response at large distances from the pointing center. For C-configuration data we used the *w*-projection algorithm (Cornwell et al. 2008) to correct for the wide-field non-coplanar baseline effect using 128 *w*-projection planes. The large images were recursively improved performing several cycles of self-calibration. This is the standard process to refine the antenna-based phase gain variations. During the last cycle, amplitude gains were also computed and applied, if possible.

<sup>1</sup> <https://casa.nrao.edu/>

<sup>2</sup> <https://science.nrao.edu/facilities/vla/docs/manuals/obsguide/modes/pol>

**Table 2.** Details of the observations. Column 1: name of the cluster with a subscript letter that specifies the relic whenever necessary; Column 2 and 3: J2000 celestial coordinates pointed in the observation; Column 4: array configuration; Column 5: observing date; Column 6: total integration time on each source.

Cluster <sub>relic</sub>	R.A.	Dec	Array Conf.	Obs. Date	Time on source [h]
8C 0212+703 <sub>E</sub>	02 <sup>h</sup> 18 <sup>m</sup> 50.0 <sup>s</sup>	+70°27′36.0″	C	03 Jun 2017	1.7
8C 0212+703 <sub>E</sub>	02 <sup>h</sup> 18 <sup>m</sup> 50.0 <sup>s</sup>	+70°27′36.0″	D	21 Mar 2017	0.8
8C 0212+703 <sub>W</sub>	02 <sup>h</sup> 14 <sup>m</sup> 31.0 <sup>s</sup>	+70°41′04.0″	C	03 Jun 2017	1.7
8C 0212+703 <sub>W</sub>	02 <sup>h</sup> 14 <sup>m</sup> 31.0 <sup>s</sup>	+70°41′04.0″	D	21 Mar 2017	0.8
Abell 3365 <sub>E</sub>	05 <sup>h</sup> 49 <sup>m</sup> 04.0 <sup>s</sup>	-21°47′05.0″	C	29 May 2017	1.7
Abell 3365 <sub>E</sub>	05 <sup>h</sup> 49 <sup>m</sup> 04.0 <sup>s</sup>	-21°47′05.0″	D	21 Mar 2017	0.4
Abell 3365 <sub>W</sub>	05 <sup>h</sup> 48 <sup>m</sup> 04.0 <sup>s</sup>	-21°52′40.0″	C	29 May 2017	1.7
Abell 3365 <sub>W</sub>	05 <sup>h</sup> 48 <sup>m</sup> 04.0 <sup>s</sup>	-21°52′40.0″	D	21 Mar 2017	0.4
PLCK G287.0+32.9	11 <sup>h</sup> 51 <sup>m</sup> 00.0 <sup>s</sup>	-28°07′17.0″	C	03 Jun 2017	1.7
PLCK G287.0+32.9	11 <sup>h</sup> 51 <sup>m</sup> 00.0 <sup>s</sup>	-28°07′17.0″	D	15 Feb 2017	0.3
ZwCl 2341.1+0000	23 <sup>h</sup> 43 <sup>m</sup> 39.7 <sup>s</sup>	+00°16′39.0″	C	02 Jul 2017	1.6
ZwCl 2341.1+0000	23 <sup>h</sup> 43 <sup>m</sup> 39.7 <sup>s</sup>	+00°16′39.0″	D	18 Feb 2017	0.8
ZwCl 2341.1+0000	23 <sup>h</sup> 43 <sup>m</sup> 44.0 <sup>s</sup>	+00°17′18.0″	C	31 Jan 2016	3.2
ZwCl 2341.1+0000	23 <sup>h</sup> 43 <sup>m</sup> 44.0 <sup>s</sup>	+00°17′18.0″	D	16 Oct 2015	1.4

In order to reduce the noise generated by bright sources in the field and to speed up the subsequent imaging processes, we subtracted all the sources external to the field of interest ( $\sim 15' \times 15'$ ) from the visibilities. Since the subtraction is not applied to cross-correlation products, polarized sources will be present outside the field of interest. This is not a problem since, both, the polarized flux density and the number of polarized sources are lower with respect to the total intensity. After the subtraction, we reduced the number of  $w$ -projection planes to 64, and we used a Briggs weighting scheme with the robust parameter set to 0.5. The latter choice was done to better image the extended emission. In the case of 8C0212, we also subtracted a bright source at the J2000 sky coordinates [02<sup>h</sup>14<sup>m</sup>32.3<sup>s</sup>; +70°49′16.7″], because its variability between the the times of C- and D-configuration observations caused imaging artifacts.

We performed a final cycle of phase and amplitude self-calibration using together the C- and D- configuration. Only the C-configuration observation was used for the analysis of PLCK287 because the addition of the D-configuration resulted in a loss of resolution and did not improve the final image quality.

In the case of ZwCl2341, we also combined the two archival observations made in the previous observing cycle. The pointing center of these observations is 1.3′ offset with respect to our observations. We checked that the flux density difference between the two observations due to the primary beam response is  $\sim 0.5\%$ . Since this difference is well below our residual calibration errors on the amplitude ( $\sim 5\%$ ), we simply shifted the phase center to the one of our observations.

The primary beam image was obtained with the `widebandpbcor` task in CASA and then used to correct the final images.

## 2.2. Polarization and RM synthesis

To produce final images of the Stokes parameters ( $I$ ,  $Q$  and  $U$ ) for the polarization analysis, we used WSCLEAN 3.0.1<sup>3</sup> (Offringa et al. 2014; Offringa & Smirnov 2017). This package is optimized to produce the wide-field frequency cubes, that will be used for the RM synthesis, as well as to take care of the wide-band to produce the images integrated over the full-band.

We produced image cubes with 64 channels at a frequency resolution of 16 MHz each. We also produced Stokes  $I$ ,  $Q$  and  $U$  images integrated over the full-band. The Stokes  $Q$  and  $U$  images were cleaned together using the `join-channels` and `join-polarizations` options. The large-scale emission of radio relics was modeled using the automated `multi-scale` option. We notice that the `multi-scale` algorithm, which is necessary to optimally image large scale emission, is not well implemented to work with the `squared-channel-joining` algorithm that should be the preferable option for cleaning Stokes  $Q$  and  $U$ . We used the Briggs weighting scheme with `robust = 0.5`. In order to perform the RM synthesis the restoring beam was forced to be the same in the full-band image and in each frequency channels, matching the lowest resolution one (i.e., at 1.02 GHz). This is done to avoid frequency-depended effects due to the variable beam size. However, we also created Stokes  $I$  images at full-resolution and in Tab. 3 we listed the characteristics of both full-resolution and low-resolution total intensity images. Some frequency channels were discarded due to their higher noise with respect to average rms noise in the other channels. Finally, each image was corrected for the primary beam calculated with CASA for the central frequency of each channel. The details of the images created in this section are listed in Tab. 3.

We refer to Brentjens & de Bruyn (2005) for a comprehensive introduction to the RM-synthesis technique. In practice, the RM synthesis performs a Fourier transform of the wavelength-squared-dependent polarization into Faraday space, obtaining the polarization as a function of the Faraday depth,  $\phi$  (see Eq. 3). In Faraday space the polarization has a peak at the Faraday depth that rotates the polarization angle of the emission. In the following, we will refer to  $\phi$  to describe the Faraday space in which the RM synthesis is performed, but we will use the more common term RM to describe the actual value derived applying this technique. This is possible because we did not detect Faraday-complex sources, for which RM and  $\phi$  do not coincide.

Similarly to the observing beam of an interferometric image, the Rotation Measure Sampling Function (RMSF) represents the instrumental response to a polarized signal in Faraday space. While the observing beam depends on the antenna configuration, the RMSF depends on the observational bandwidth and on the width of the sub-bands in the  $\lambda^2$ -space. Brentjens & de Bruyn (2005) obtained approximated formulas to compute the

<sup>3</sup> <https://gitlab.com/aroffringa/wsclean>

**Table 3.** Details of the images. Column 1: name of the cluster with a subscript letter that specifies the relic whenever necessary; Column 2: JVLA array configuration used to produce the image; Column 3: robust parameter used for the Briggs weighting scheme; Column 4: FWHM of the tapering function used to produce the image; Column 5: FWHM of the major and minor axis of the resolution beam of the image; Column 6: rms noise of the total intensity image; Column 7: rms noise of the polarized intensity image produced from the Q and U images integrated over the full-band; Column 8: average noise in the polarized intensity image computed through RM-synthesis. See Sec. 2.2 for the details on the noise calculation. Column 9: reference to the figure in this paper.

Cluster <sub>relic</sub>	Array Conf.	Robust	Taper	Beam	$\sigma_I$ [μJy/beam]	$\sigma_{QU}$ [μJy/beam]	$\langle\sigma_{\tilde{Q}\tilde{U}}\rangle$ [μJy/beam/RMSF]	Fig.
8C 0212+703 <sub>E</sub>	C+D	0.5	–	18.2″×12.2″	20	–	–	1,2
	C+D	0.5	20″	29″×29″	35	18	15	1,2
8C 0212+703 <sub>W</sub>	C+D	0.5	–	18.6″×12.8″	22	–	–	1,3
	C+D	0.5	20″	33″×33″	35	15	17	1,3
Abell 3365 <sub>E</sub>	C+D	0.5	–	21.0″×10.6″	28	–	–	4, 5
	C+D	0.5	–	30″×30″	28	13	16	4, 5
Abell 3365 <sub>W</sub>	C+D	0.5	–	21.0″×10.7″	25	–	–	4
	C+D	0.5	–	31″×31″	28	16	19	4
PLCK G287.0+32.9	C	0.5	–	28.4″×11.7″	33	–	–	6, 7
	C	0.5	–	41″×41″	50	11	14	6, 7
ZwCl 2341.1+0000	C+D	0.5	–	16.3″×13.5″	17	–	–	8, 9, 10
	C+D	0.5	–	28″×28″	18	8	11	8, 9, 10

resolution in Faraday space,  $\delta\phi$ , the maximum observable Faraday depth,  $|\phi_{\max}|$ , and the largest observable scale in Faraday space,  $\Delta\phi_{\max}$  (i.e., the depth and the  $\phi$ -scale at which sensitivity has dropped to 50 %). Therefore, considering our observing parameters, we have:

$$\delta\phi \sim 45 \text{ rad m}^{-2}, \quad (5)$$

$$|\phi_{\max}| \sim 535 \text{ rad m}^{-2}, \quad (6)$$

$$\Delta\phi_{\max} \sim 143 \text{ rad m}^{-2}. \quad (7)$$

We performed the RM synthesis on the  $Q(\nu)$  and  $U(\nu)$  frequency cubes with `pyrmsynth`<sup>4</sup>. Faraday cubes were created between  $\pm 1000 \text{ rad m}^{-2}$  in order to have a wide range outside our  $|\phi_{\max}|$  to compute the noise from the spectra. We used equal weights for all the channels and we imposed a spectral correction using an average spectral index  $\alpha = 1$ . We masked the  $Q(\nu)$  and  $U(\nu)$  images using the  $3\sigma$  threshold applied to the full-band total intensity images having the same resolution as the frequency cubes (see Tab. 3 for the rms noise of these images). We also performed the RM clean down to the same threshold (see Heald 2009, for the RM clean technique).

Applying the RM synthesis we obtained, in each pixel of the image, the reconstructed Faraday dispersion function, or Faraday spectrum,  $\tilde{F}(\phi)$ , which describes the polarization as a function of the Faraday depth. We also obtained the reconstructed  $\tilde{Q}(\phi)$ ,  $\tilde{U}(\phi)$  cubes in Faraday space. For each pixel we measured the noise of  $\tilde{Q}(\phi)$  and  $\tilde{U}(\phi)$  computing the rms,  $\sigma_{\tilde{Q}}$  and  $\sigma_{\tilde{U}}$ , in the external ranges of the spectrum: at  $|\phi| > 500 \text{ rad m}^{-2}$ . This Faraday depth range is outside of the sensitivity range of our observations and should be free from the contamination of residual side-lobes. Since  $\sigma_{\tilde{Q}} \sim \sigma_{\tilde{U}}$ , we estimated the noise of each pixel of the polarization observations as  $\sigma_{\tilde{Q}\tilde{U}} = (\sigma_{\tilde{Q}} + \sigma_{\tilde{U}})/2$  (see also Hales et al. 2012). By definition,  $\sigma_{\tilde{Q}\tilde{U}}$  is in units of Jy/beam/RMSF. In Tab. 3, we list the value of  $\langle\sigma_{\tilde{Q}\tilde{U}}\rangle$ , where the average is computed over the image using all the unmasked pixels.

We fitted pixel-by-pixel a parabola around the main peak of the Faraday dispersion function. From the value of the Far-

aday depth at the peak we obtained the  $\text{RM} = \phi_{\text{peak}}$ , while from  $|\tilde{F}(\phi_{\text{peak}})|$  we obtained the polarized intensity. For our analysis, we considered only pixels with  $|\tilde{F}(\phi_{\text{peak}})| > 6\sigma_{\tilde{Q}\tilde{U}}$ . This corresponds to a Gaussian significance level of about  $5\sigma$  (see Hales et al. 2012).

We computed polarization intensity images using the peak of the Faraday dispersion function, and correcting for the Ricean bias as  $P = \sqrt{|\tilde{F}(\phi_{\text{peak}})|^2 - 2.3\sigma_{\tilde{Q}\tilde{U}}^2}$  (George et al. 2012). We then obtained fractional polarization images dividing the  $P$  images (with the  $6\sigma_{\tilde{Q}\tilde{U}}$  threshold) by the full-band Stokes  $I$  images (masked at the  $3\sigma$  level). In order to check the RM synthesis results we also produced integrated polarization images using the  $Q$  and  $U$  images obtained using the full-band and applying the usual formula  $P = \sqrt{Q^2 + U^2}$ . The rms noise of these images is listed in Tab. 3 as  $\sigma_{QU}$ .

In order to compute the upper limits to the fractional polarization for those sources which were not detected in polarization we created a map of  $6\sigma_{\tilde{Q}\tilde{U}}/I$ . We considered as an upper limit the minimum of all values reached in this map within the relic region. This upper limit is more stringent than the one calculated from the average value across the source, but it is comparable with fractional polarization values which are computed only from the brightest pixels.

From the reconstructed values of  $Q$  and  $U$  at  $\phi_{\text{peak}}$  we can also recover the intrinsic polarization angle (i.e., corrected for the value of RM determined by  $\phi_{\text{peak}}$ ),  $\chi_0$ , as:

$$\chi_0 = \chi(\lambda_0^2) - \phi_{\text{peak}}\lambda_0^2 = \frac{1}{2} \arctan \frac{\tilde{U}(\phi_{\text{peak}})}{\tilde{Q}(\phi_{\text{peak}})} - \phi_{\text{peak}}\lambda_0^2, \quad (8)$$

where  $\lambda_0$  is the central wavelength in the sampled wavelength-squared space. The magnetic field projected on the plane of the sky is then obtained from  $\chi_0$ .

The pixel-wise uncertainty on  $\phi_{\text{peak}}$  (and thus on the RM value in the single pixel) is derived following Brentjens & de Bruyn (2005), where:

$$\sigma_{\phi} = \frac{\delta\phi}{2P/\sigma_{\tilde{Q}\tilde{U}}}, \quad (9)$$

<sup>4</sup> <https://github.com/mrbell/pyrmsynth>

that is the FWHM of the RMSF divided by twice the signal-to-noise of the detection (see also Schnitzeler & Lee 2017).

We corrected the RM values for the Galactic foreground. We computed the median Galactic RM (GRM) in a 1 degree diameter circle around the galaxy cluster from Hutschenreuter et al. (2021). GRM values are listed in Tab. 1. Finally we subtracted the GRM value from our RM maps to obtain the residual RM (RRM). In the following, we will consider RRM values of extra-galactic origin. Since the RM dispersion within 1 degree computed from the Hutschenreuter et al. (2021) map is lower than  $6 \text{ rad m}^{-2}$  for the four considered clusters, the residual Galactic contribution on the angular size of radio relics (few arcminutes) should be well below this value.

In the following Section, we will quote only observed RRM values. This values can differ from the intrinsic RM value in the rest-frame of the Faraday screen due to the cosmological expansion. This difference can be particularly important for high-redshift sources (see e.g., Carretti et al. 2022). Assuming that the whole extra-galactic Faraday rotation occurs at the source redshift, i.e. in the ICM of the galaxy cluster, the rest-frame RRM is  $\text{RRM}(1+z)^2$ , with the  $z$  of the cluster. In Sec. 4 we will consider rest-frame RRM values.

### 3. Results

In this Section we show total intensity, polarization, and RRM images obtained for the four galaxy clusters. For 8C0212 and A3365 we created total intensity composite images of the two separate pointings only for visualization.

The polarized intensity images integrated over the full band and masked at  $6\sigma_{QU}$  are shown with filled contours on top of the total intensity images, in order to show the regions where polarized emission was detected. With respect to polarized intensity images obtained from RM synthesis, these images show much smoother detected regions since the masking is made with an average rms value while for the RM synthesis we masked on a per-pixel basis. Furthermore, they often have a lower rms noise level (see Tab. 3) because the RM synthesis introduces additional noise that is collected in the Faraday spectrum. On the other hand, full-band integrated images suffer from in-band depolarization and are therefore less accurate for polarization measurements. Hence, we used them only for better visualization.

We detected extended polarized emission only for two out of eight radio relics, namely the eastern relic of Abell 3365 and the southern relic of PLCK287. For other three relics, i.e. the two relics in 8C0212 and the southern relic of ZwCl2341, we only detected few patches of polarized emission. The remaining three relics are unpolarized up to our detection threshold.

#### 3.1. 8C 0212+703 (CIG 0217+70)

The galaxy cluster 8C0212 shows few patches of polarized emission at the position of the E1 source and of the brightest part of the western relic (see Fig. 1).

Source E is close, at least in projection, to the eastern radio relic and was distinguished in two components (E1 and E2) by Hoang et al. (2021) on the basis of their morphology. E1 has a double lobed structure, typical of a Fanaroff-Riley type I radio galaxy, with an optical counterpart in Pan-STARRS. The southern lobe is bent towards the E direction while the northern one is bent towards NW where it merge with E2 (see also Fig. 2). E2 has an elongated structure and spectral index steepening towards the cluster center (Hoang et al. 2021). Spectral index vari-

ations between E1 and E2 suggest a possible shock-induced re-acceleration of the fossil plasma ejected by the southern AGN.

We detected polarized emission from the lobes of the radio galaxy (source E1, see Fig. 2). The average fractional polarization is  $16 \pm 2 \%$  and  $17 \pm 2 \%$  in the northern and southern lobes, respectively, but it reaches values of 60 % in the eastern extension of the southern lobe. Magnetic field vectors are aligned with the main axis of the northern lobe while they get aligned in the perpendicular direction towards the eastern extension up to the edge, where the fractional polarization reaches its maximum. Interestingly, at this position the spectral index becomes flatter, as reported by Hoang et al. (2021). This suggests that in this region a physical process is simultaneously accelerating particles and aligning the plane-of-the-sky magnetic field components. The presence of a shock wave, as already proposed by Hoang et al. (2021) to explain the spectral index properties of E2, would furnish a good explanation also for the eastern extension of the southern lobe. However, without deeper X-ray images able to detect the presence of a shock, this remains an hypothesis. Furthermore, the fact that E2 is not detected in polarization with an upper limit of 13 % challenges this interpretation.

The median RRM in the northern lobe is  $-28 \text{ rad m}^{-2}$  with a standard deviation,  $\sigma_{\text{RM}}$ , of  $2 \text{ rad m}^{-2}$ . The brightest part of the southern lobe has similar values of RRM, while the RRM increases to a median value of  $-20 \text{ rad m}^{-2}$  in the eastern extension (see Fig. 2, right panel). This difference could be attributed to both projection effects (with the brightest part of the lobe being closer), magnetic field strength and/or thermal electron density variations or to magnetic field reversals.

We did not detect polarization from sources D, F, and G. These sources are very faint and only partially detected by our observations. The upper limit to their fractional polarization is: 28 %, 22 % and 26 %, respectively.

We detected few patches of polarized emission arising from the western radio relic (source C, see Fig. 3). The average fractional polarization here is  $12 \pm 2 \%$  with a maximum values of  $\sim 23 \%$  while the RRM has a median value of  $-7 \text{ rad m}^{-2}$  and  $\sigma_{\text{RM}} = 10 \text{ rad m}^{-2}$ . Magnetic field vectors are broadly aligned with the main axis of the radio emission. Overall, the detection of polarized emission confirm the identification of the C source with a radio relic. However, considering the elongated shape of this radio relic and its peripheral position ( $\sim 2.4 \text{ Mpc}$  from the cluster center), we would expect to detect higher fractional polarization values. This will be discussed in Sec. 4.1.

#### 3.2. Abell 3365

The elongated eastern radio relic of A3365 shows extended polarized emission while the western relic remains undetected in polarization (see Fig. 4).

The zoomed view of the eastern relic is shown in Fig. 5. The polarized emission is detected from the brightest region of the relic, but is more patchy with respect to the total intensity emission. The average fractional polarization in the detected regions is  $9.0 \pm 0.8 \%$ , reaching a maximum value of 18 %. Polarization vectors are parallel to the main axis of the relic only in the northern part, while they bent and become perpendicular towards the south. The median RRM is  $-11 \text{ rad m}^{-2}$  and  $\sigma_{\text{RM}} = 11 \text{ rad m}^{-2}$ . The RM values are more scattered in the northern part of the relic.

The western relic is much fainter than the eastern one and it has not the classical arc-like shape. The upper limit to its fractional polarization is 8 %. Its low fractional polarization could



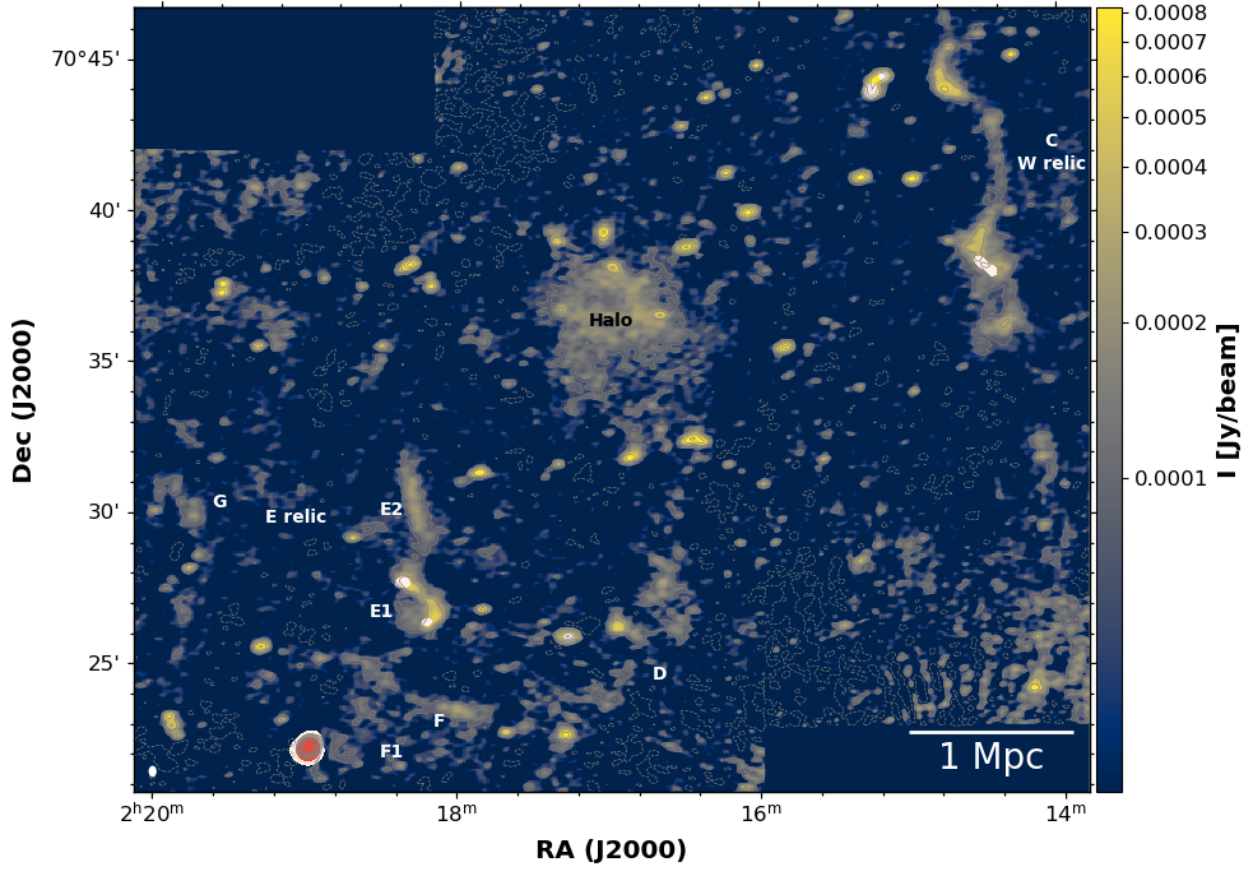


**Fig. 1.** The galaxy cluster 8C0212. The blue-yellow color scale shows the full-resolution total intensity image at the central frequency of 1.5 GHz. Contours start at  $3\sigma$  (with  $\sigma = 25 \mu\text{Jy/beam}$ ) and increase by a factor of 2. The dashed contour shows the  $-3\sigma$  level. Filled white-red contours show the polarized intensity image integrated over the full band with  $[6,12,24,96]\sigma_{QU}$  levels. Beam size and  $\sigma_{QU}$  values are listed in Tab. 3. Diffuse sources are labeled following Hoang et al. (2021).

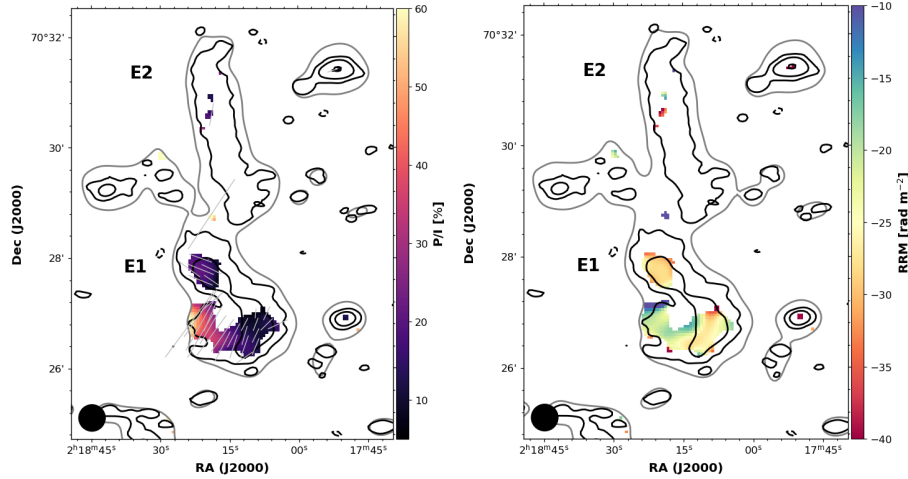


**Fig. 2.** Fractional polarization and residual RM (i.e., corrected for Galactic Faraday rotation) images of source E in the eastern side of 8C0212. In the left-hand panel, gray vectors show the magnetic field direction and their length is proportional to the fractional polarization value. Black contours are  $[-3,3,12]\sigma_I$  of the high-resolution total intensity image while the gray contour shows the  $3\sigma_I$  of the low-resolution total intensity image used to compute the fractional polarization. Only pixels above the  $6\sigma_{\overline{QU}}$  are shown. Rms noise levels and beam sizes are listed in Tab. 3.

be due to projection effects. This will be further discussed in Sec. 4.1.

### 3.3. PLCK G287.0+32.9 (PSZ2 G286.98+32.90)

We detected diffuse polarized emission from the southern radio relic in PLCK287 (see Fig. 6 and Fig. 7). Polarization vectors are well aligned with the main axis of this relic and the fractional polarization reaches the 31 % with an average value of  $20 \pm 1$  %.



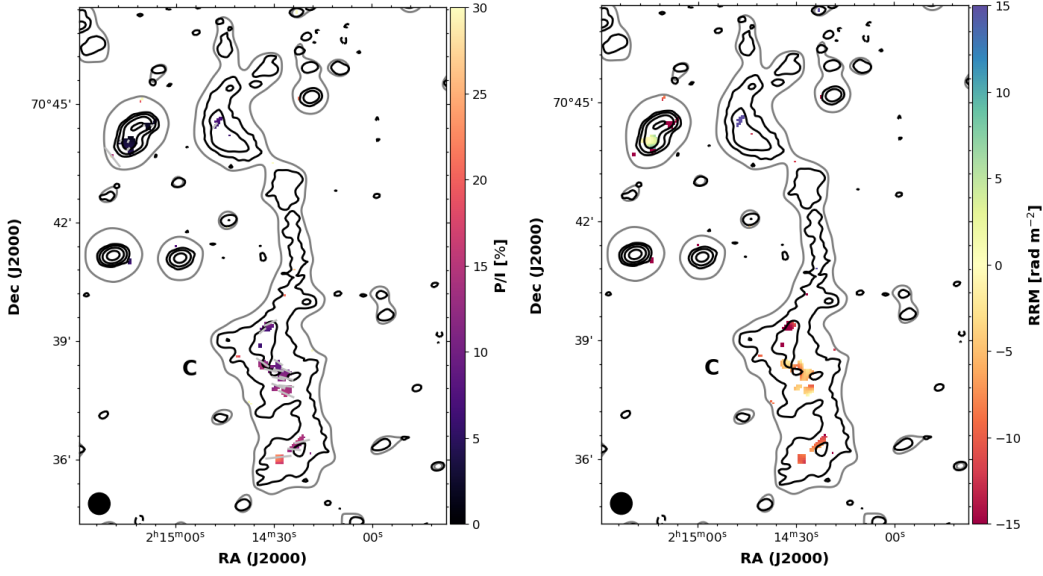


**Fig. 3.** Fractional polarization and residual RM (i.e., corrected for Galactic Faraday rotation) images the western relic of 8C0212 (source C). In the left-hand panel, gray vectors show the magnetic field direction and their length is proportional to the fractional polarization value. Black contours are  $[-3, 3, 12, 48, 192]\sigma_I$  of the high-resolution total intensity image while the gray contour shows the  $3\sigma_I$  of the low-resolution total intensity image used to compute the fractional polarization. Only pixels above the  $6\sigma_{QU}$  are shown. Rms noise levels and beam sizes are listed in Tab. 3.

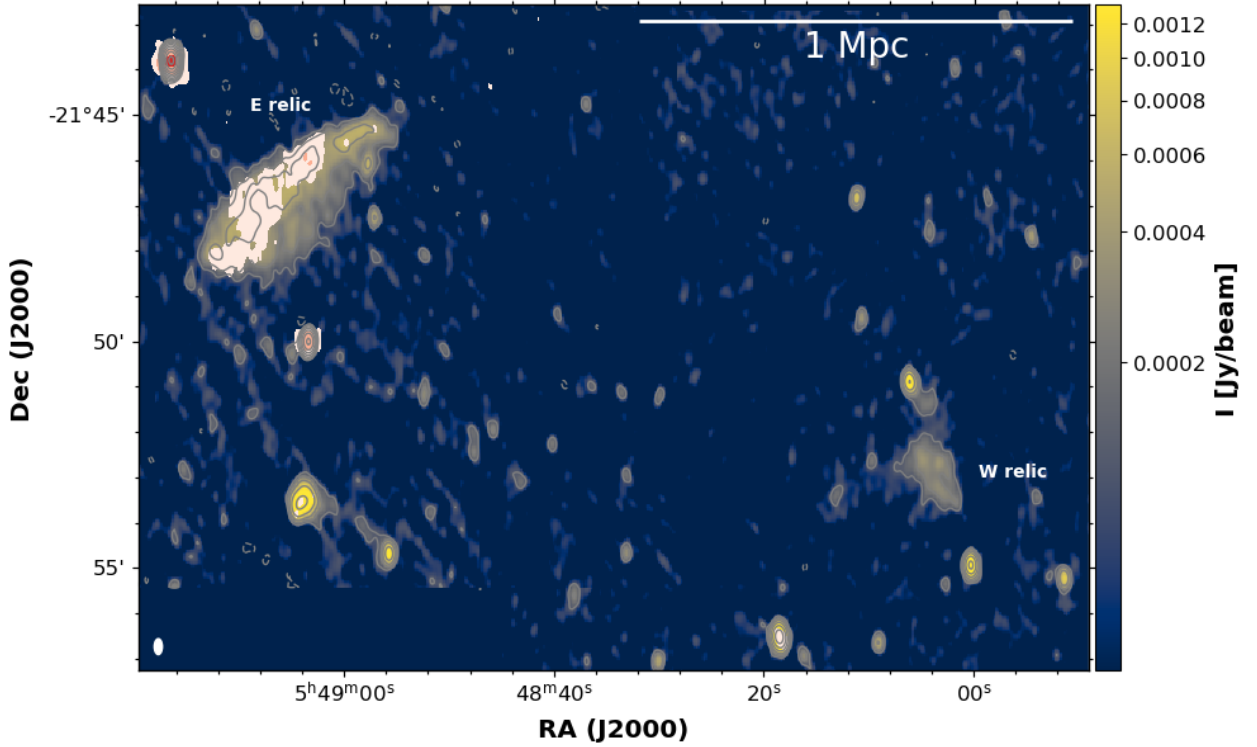


**Fig. 4.** The galaxy cluster A3365. The blue-yellow color scale shows the full-resolution total intensity image at the central frequency of 1.5 GHz. Contours start at  $3\sigma$  (with  $\sigma = 40 \mu\text{Jy/beam}$ ) and increase by a factor of 2. The dashed contour shows the  $-3\sigma$  level. Filled white-red contours show the polarized intensity image integrated over the full band with  $[6, 12, 24, 48]\sigma_{QU}$  levels. Beam size and  $\sigma_{QU}$  values are listed in Tab. 3. The two relics are labeled.

We have also detected few patches of polarized emission arising from the southern extension of this relic, previously noticed by Bonafede et al. (2014), thus supporting its connection to the radio relic. The median RRM at the southern relic is  $5 \text{ rad m}^{-2}$  with  $\sigma_{\text{RM}} = 8 \text{ rad m}^{-2}$ . We observed a gradient of decreasing RRM going from the western side of the relic to the east, where the RRM approaches zero (see Fig. 7). This behavior suggests

a possible inclination of the relic on the plane of the sky, with the western part lying deeper in the ICM and experiencing more Faraday rotation. Galactic RM variation across the sources on arcminutes-scales cannot be excluded.

We also detected the polarized lobes of the radio galaxy in the north of the cluster (see Fig. 6). The southern lobe of the radio galaxy is connected to the northern radio relic but polar-

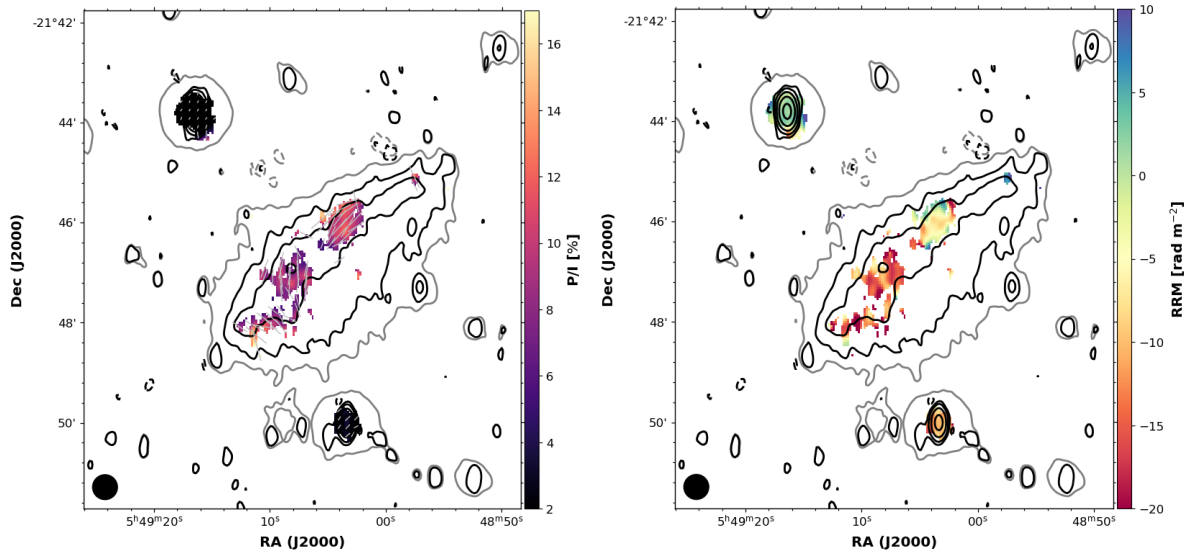


**Fig. 5.** Fractional polarization and residual RM (i.e., corrected for the Galactic Faraday rotation) images of the eastern relic of A3365. In the left-hand panel, gray vectors show the magnetic field direction and their length is proportional to the fractional polarization value. Black contours are  $[-3, 3, 12, 48, 192, 768]\sigma_I$  of the high-resolution total intensity image while the gray contour shows the  $\pm 3\sigma_I$  of the low-resolution total intensity image used to compute the fractional polarization. Only pixels above the  $6\sigma_{\overline{Q\overline{U}}}$  are shown. Rms noise levels and beam sizes are listed in Tab. 3.

ization was not detected neither from the relic nor from the radio bridge between the two sources. The upper limit to the fractional polarization of the northern radio relic is 0.8 %. Indeed this relic is very bright and if any polarization was present we should have detected it. We know from Bonafede et al. (2014) that the northern relic is close in projection to the galaxy cluster center and to its X-ray emission peak. It is possible that it is located in behind the bulk of the ICM and that the external Faraday dispersion totally depolarize the signal within our resolution beam ( $\sim 220$  kpc, see also Sec. 4.1). The lobes of the radio galaxy are far away from the cluster center and we were able to detect their polarized emission. Bonafede et al. (2014) did not find the optical counterpart of this source using the Wide Field Imager (WFI). We also searched for a counterpart with redshift estimate in the NED database, without success. However, the RRM of the radio galaxy lobes are similar to those of the nearest galaxy which is a confirmed galaxy cluster member (being  $19 \text{ rad m}^{-2}$ ,  $25 \text{ rad m}^{-2}$  and  $32 \text{ rad m}^{-2}$  the median RRM of the north-western lobe, south-eastern lobe and of the nearest galaxy cluster member detected in polarization, respectively, and  $21 \text{ rad m}^{-2}$ ,  $19 \text{ rad m}^{-2}$  and  $16 \text{ rad m}^{-2}$ , their RM dispersion). This support the idea that the radio galaxy is in the same environment of the radio relic.

### 3.4. ZwCl 2341.1+0000

Our total intensity image of ZwCl2341 (Fig. 8) is similar to those recently presented by Parekh et al. (2022) and obtained with the MeerKAT radio telescope at 1.28 GHz. However, we do not confirm their marginal detection of extended emission in the galaxy cluster center.

The northern radio relic of the ZwCl2341 system is unpolarized in our observations. Its polarization fraction has an upper limit of 5 %. A zoomed view of this relic and of the surrounding sources is shown in Fig. 9. A cluster radio galaxy to the east of the relic (source A in Fig. 8), possibly classified as an head-tail source by van Weeren et al. (2009), has an average fractional polarization of  $7.7 \pm 0.7$  % with a maximum value of 13 %. An-

other polarized source (source B) is observed towards the cluster center and its high RM dispersion ( $94 \text{ rad m}^{-2}$ ) suggests that it is located deeper in the ICM. It is in fact a member of this galaxy cluster (van Weeren et al. 2009).

The southern relic shows few patches of polarized emission with average fractional polarization of  $13 \pm 2$  % (see Fig. 10). There are few pixels with fractional polarization reaching the 33 % but the polarized emission is concentrated in the brightest relic region in the south, which has a roundish morphology and a maximum fractional polarization of 18 %. We checked that this is not a point-source since it disappears increasing the image resolution. The median RRM is  $-2 \text{ rad m}^{-2}$  and  $\sigma_{\text{RM}} = 22 \text{ rad m}^{-2}$ .

Giovannini et al. (2010) reported the detection of polarized emission all over the two relics and also in the region between them using VLA low resolution images ( $83'' \times 75''$ ,  $\sim 330$  kpc at the cluster's redshift) at 1.4 GHz. They found 15 % fractional polarization in the northern relic and 8 % in the southern one. While the value found in the southern relic is consistent with our measurements (considering beam-depolarization), our non-detection of the northern relic is at odds with their findings. We suggest that this is due to the contamination from the polarized emission of the head-tail radio galaxy to the east of the relic (source A in Fig. 8) which could be under-subtracted in low-resolution images. In our images the fractional polarization of the AGN reaches the 13 % and the magnetic field direction at the source is consistent with the one obtained by Giovannini et al. (2010). Also, we checked that using only the D configuration and integrating over the full band we can recover polarized emission at 5 % level from the northern relic, but this emission is not present after the RM synthesis due to the low signal-to-noise. Benson et al. (2017) measured the fractional polarization of the two relics in the 2 – 4 GHz band obtaining 5 % for the northern relic and 8 % for the southern one. In this case, the value found in the northern relic is consistent with our upper limit while the southern relic show a lower polarization fraction. This could be due to the fact that we only detected polarized emission from the brightest and most polarized regions of the relic. The image produced in the 2 – 4 GHz band by Benson et al. (2017) shows polarized emission all over the relic possibly catching also low

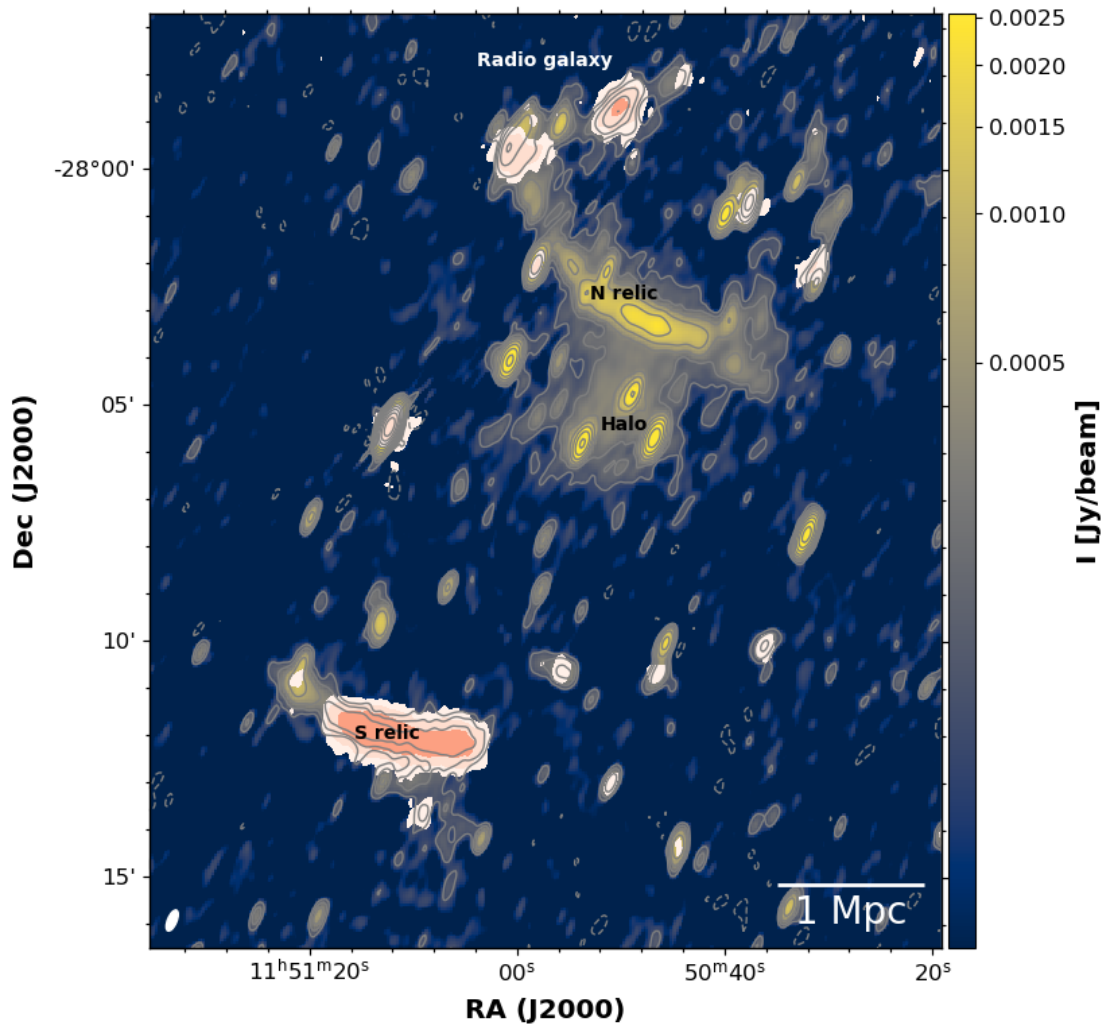


**Fig. 6.** The galaxy cluster PLCK287. The blue-yellow color scale shows the full-resolution total intensity image at the central frequency of 1.5 GHz. Contours start at  $3\sigma$  (with  $\sigma = 33 \mu\text{Jy/beam}$ ) and increase by a factor of 2. The dashed contour shows the  $-3\sigma$  level. Filled white-red contours show the polarized intensity image integrated over the full band with  $[6, 12, 24, 48, 96]\sigma_{QU}$  levels. Beam size and  $\sigma_{QU}$  values are listed in Tab. 3. Notable diffuse radio sources are labeled.

fractional polarization regions. A polarization study performed combining L- and S-band measurements would be necessary to deeply investigate this difference and to unveil possible complex Faraday structures in this relic.

However, given the disturbed structure of this cluster, the non-detection of surface brightness edges from deep *Chandra* observations (Zhang et al. 2021) and the possible presence of a secondary merger along the line-of-sight (Golovich et al. 2019b), it is very likely that these relics are not seen edge-on and that projection effects play a role in determining their depolarization fraction. This is also supported by the RM dispersion of the southern relic which is the highest observed in our sample.

#### 4. Discussion

In this Section we compare our results with literature information about double radio relics and with state-of-the-art of MHD simulations.

In Tab. 4, we made a compilation of all known double radio relics in the literature. For each of them we listed, when available, fractional polarization (average and maximum) and Faraday rotation (average/median subtracted from the Galactic

foreground and dispersion). We computed here RRM and  $\sigma_{RM}$  values as measured in the source rest-frame, assuming that all the residual RM and RM dispersion are generated at the galaxy cluster's redshift and therefore we multiplied the observed values by  $(1+z)^2$  (see also Sec. 2.2). This operation is needed to compare observational results with simulations although it is often neglected in the literature. We considered only observations at 1.4 GHz in order to compare with our observations (with the only exception of the El Gordo galaxy cluster for which 1.4 GHz observations are not available).

Our collection resulted in 22 double radio relics systems. We found polarization information for 15 clusters but Faraday rotation measurements are available only for 9 of them. Therefore, with this work we have almost doubled the number of double relics galaxy clusters with RM information. The results reported in the table highlight that a lot of information is still missing in order to have a complete view about the polarization properties of double radio relic systems.

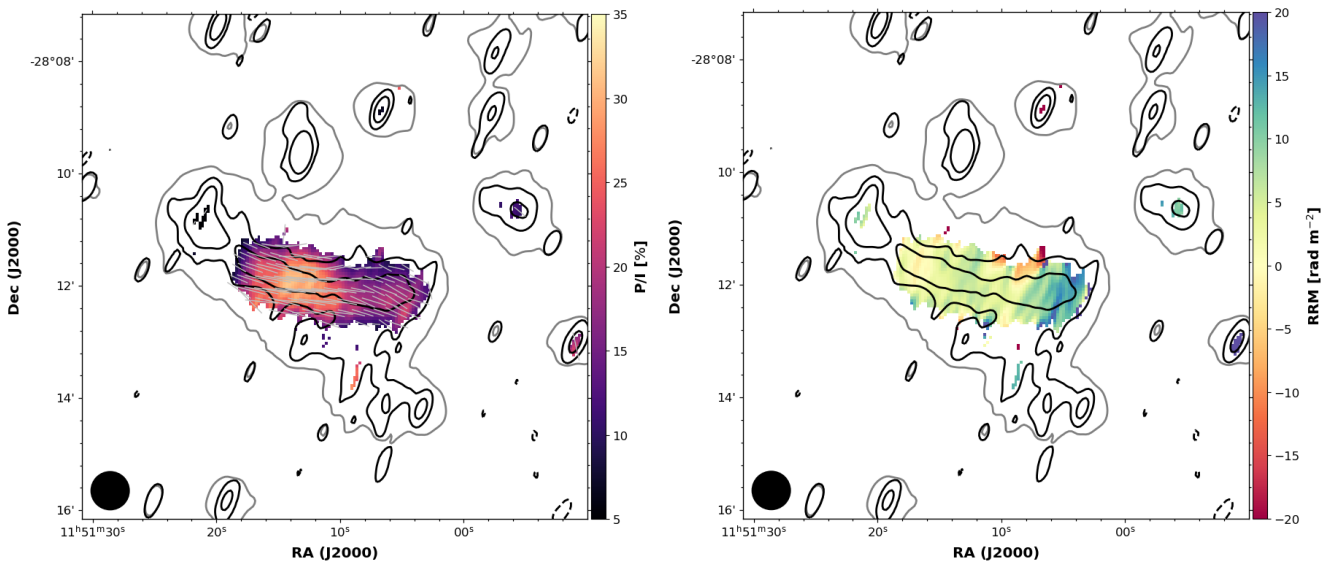


**Fig. 7.** Fractional polarization and residual RM (i.e., corrected for the Galactic Faraday rotation) images of the southern relic of PLCK287. In the left-hand panel, gray vectors show the magnetic field direction and their length is proportional to the fractional polarization value. Black contours are  $[-3, 3, 12, 48, 192]\sigma_I$  of the high-resolution total intensity image while the gray contour shows the  $3\sigma_I$  of the low-resolution total intensity image used to compute the fractional polarization. Only pixels above the  $6\sigma_{\overline{Q}}$  are shown. Rms noise levels and beam sizes are listed in Tab. 3.

#### 4.1. Fractional polarization and depolarization effects

High levels of fractional polarization are expected from radio relics, in particular for those seen edge-on, such as double radio relics. This is due to the plane-of-the-sky magnetic field compression operated by the passing shock wave (Ensslin et al. 1998; Iapichino & Brüggen 2012). Recent and advanced MHD simulations show that magnetic field alignment, and therefore high levels of fractional polarization, can be produced by the compression of a randomly oriented magnetic field, which is the natural outcome of the turbulent evolution in the ICM (Wittor et al. 2019; Domínguez-Fernández et al. 2021).

Using the simple analytical formula derived by Ensslin et al. (1998, Eq. 22) and assuming DSA, a radio relic generated by a planar shock wave with Mach number 3 propagating along the plane of the sky reaches an average polarization fraction of 62%. Lower viewing angles lead to lower polarization fractions. Clearly, not all double radio relics are perfectly seen edge-on and projection effects could have a role in determining their polarization fraction. Sometimes this is also suggested by their asymmetry with respect to the merger axis or non-arc-like shape, such as the western relic in A3365 (Fig. 4) and the relics in ZwCl2341 (Fig. 8). However, on average, double radio relics should constitute a more uniform sample with respect to the viewing angle and merger geometry compared to single or multiple radio relic systems (Golovich et al. 2019b).

The average fractional polarization of known double radio relics is in the range 9 – 33 % (with average 19 %) while the maximum value spans between 10 % and 70 % (with average 40 %). Hence, the majority of double radio relics shows lower values of maximum and average polarization with respect to the average value expected for radio relics seen edge-on, if depolarization is not present.

However, both filamentary polarized structures and fractional polarization gradients are found in radio relics when they are observed at high-resolution (i.e.  $\leq 20$  kpc, Di Gennaro et al. 2021; Rajpurohit et al. 2022b; de Gasperin et al. 2022). In particular, Di Gennaro et al. (2021) found a clear gradient across the Sausage relic with intrinsic fractional polarization decreas-

ing towards the cluster center. This trend can be reproduced by simulations considering a  $M = 3$  shock wave propagating through a medium perturbed by decaying subsonic turbulence in the ICM (Domínguez-Fernández et al. 2021). This trend can be also reproduced with semi-analytical models based on shock compression of a small-scale tangled magnetic field, although this result was found to strongly depend on the magnetic field strength (Hoeft et al. 2022). Furthermore, the morphology of simulated polarized emission resembles the structures of the underlying turbulent ICM, creating threads and filaments (Domínguez-Fernández et al. 2021). The mixing of different polarized structures within the observing beam leads to lower value of average fractional polarization than what is predicted by the analytical formula provided by Ensslin et al. (1998). This effect is particularly significant if the physical scale corresponding to the beam size is of the same order of the reversal (or correlation) scale of magnetic field structures.

Furthermore, linearly polarized emission can be depolarized by several effects, in particular:

- beam depolarization, caused by the mixing of several lines-of-sight having different polarization angles within the resolution beam;
- differential Faraday rotation, when a region of space contains relativistic electrons, thermal electrons and regular magnetic fields and the polarization angle of the radiation emitted from the farthest layer is more Faraday-rotated than that from the nearest one;
- internal and/or external Faraday dispersion, caused by the presence of turbulent and filamentary magnetic fields inside or in front of the radio relic emission that produce an RM dispersion along the line-of-sight and/or within the resolution beam.

In principle, the RM-synthesis can overcome both differential Faraday rotation and internal Faraday dispersion because it distinguishes polarized emissions having different Faraday depth along the line-of-sight. In none of our radio relics we detected multiple Faraday depth peaks and therefore we can exclude the



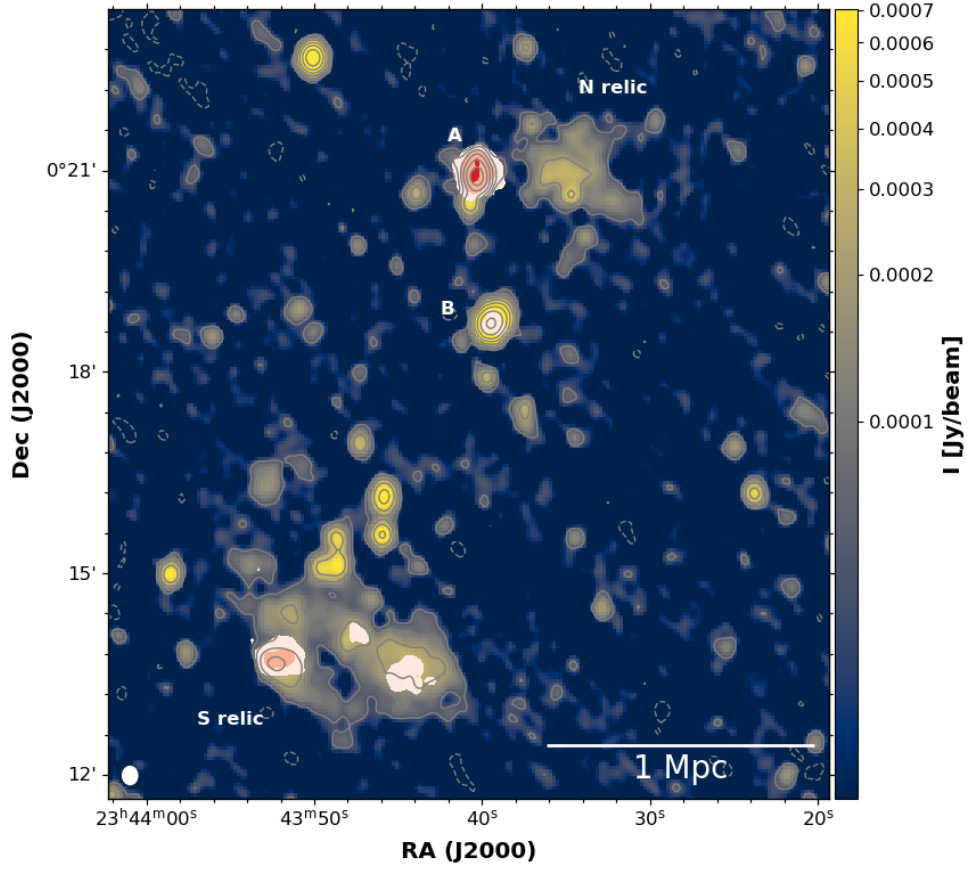


**Fig. 8.** The galaxy cluster ZwCl2341. The blue-yellow color scale shows the full-resolution total intensity image at the central frequency of 1.5 GHz. Contours start at  $3\sigma$  (with  $\sigma = 17 \mu\text{Jy/beam}$ ) and increase by a factor of 2. The dashed contour shows the  $-3\sigma$  level. Filled white-red contours show the polarized intensity image integrated over the full band with  $[6,12,24,48]\sigma_{QU}$  levels. Beam size and  $\sigma_{QU}$  values are listed in Tab. 3. The two radio relics and two radio galaxies detected in polarization are labeled.

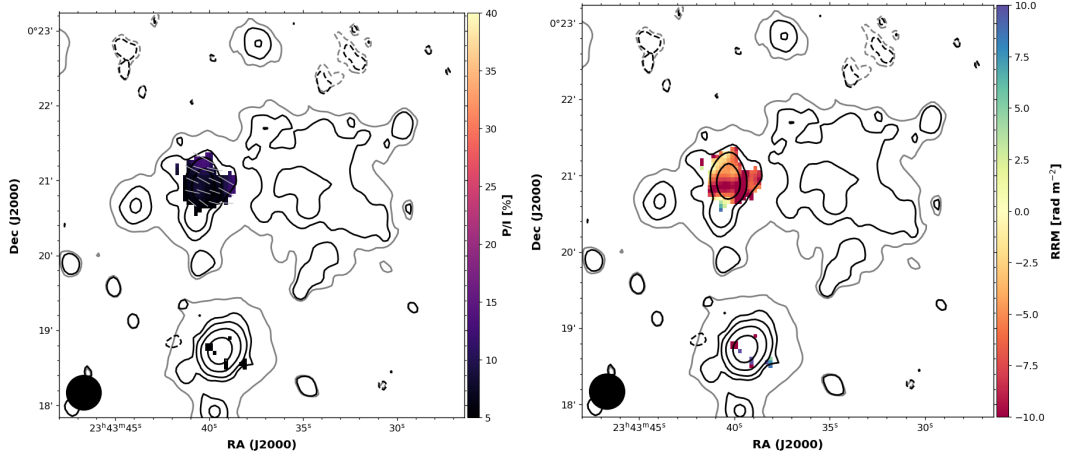


**Fig. 9.** Fractional polarization and residual RM (i.e., corrected for the Galactic Faraday rotation) images centered on the northern relic of ZwCl2341. In the left-hand panel, gray vectors show the magnetic field direction and their length is proportional to the fractional polarization value. Black contours are  $[-3,3,12,48]\sigma_I$  of the high-resolution total intensity image while the gray contour shows the  $\pm 3\sigma_I$  of the low-resolution total intensity image used to compute the fractional polarization. Only pixels above the  $6\sigma_{QU}$  are shown. Rms noise levels and beam sizes are listed in Tab. 3. The only detected sources in polarization are two cluster's radio galaxies.

presence of multiple emission layers with RM dispersion larger than our resolution in Faraday space, i.e.  $45 \text{ rad m}^{-2}$ . However, a smaller Faraday dispersion would be undetectable by our observations and only with a larger bandwidth we would be able to recover it.

Beam depolarization due to the mixing of intrinsically different polarization angles or to external Faraday dispersion can be avoided only with observations performed at higher resolution. However, high-resolution observations are less sensitive to the faint extended emission that characterizes radio relics. A trade-off between depolarization and loss of sensitivity to the extended

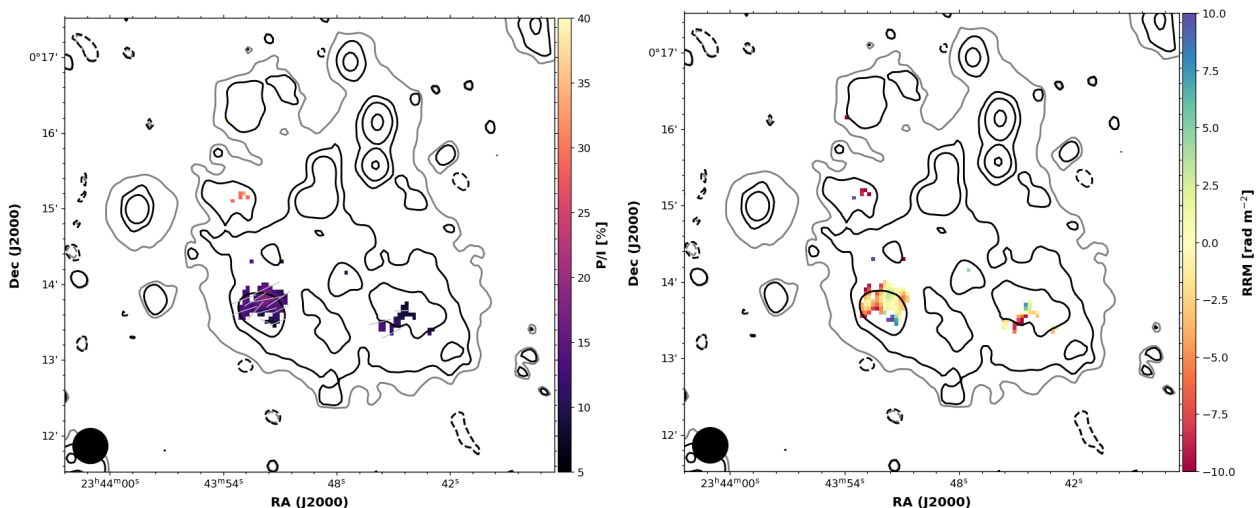


**Fig. 10.** Fractional polarization and residual RM (i.e., corrected for the Galactic Faraday rotation) images of the southern relic of ZwCl2341. In the left-hand panel, gray vectors show the magnetic field direction and their length is proportional to the fractional polarization value. Black contours are  $[-3, 3, 12, 48]\sigma_I$  of the high-resolution total intensity image while the gray contour shows the  $\pm 3\sigma_I$  of the low-resolution total intensity image used to compute the fractional polarization. Only pixels above the  $6\sigma_{\overline{Q\overline{U}}}$  are shown. Rms noise levels and beam sizes are listed in Tab. 3.

emission has to be found in order to observe the polarized emission of radio relics.

Since beam depolarization should be reduced by high-resolution observations, we want to explore if lower fractional polarization values are found in double relics observed at lower resolution. We listed in Tab. 4 the major and minor axis of the observing beam for each observation and the corresponding physical size. The distribution of fractional polarization values is plotted against the physical resolution of the observation in Fig. 11. The markers are color-coded with the distance of each relic from the X-ray centroid of the cluster (also listed in Tab. 4). We do not observe a strong correlation between the two quantities with a Spearman correlation coefficient of -0.35 using the average polarization values, and 0.02 using the maximum fractional polarization. This suggests that the physical resolution of the observation is not the main driver of depolarization effects in current observations. We do not observe a correlation either with the relic's distance from the cluster center, which should account for larger RM variations within the beam.

Domínguez-Fernández et al. (2021) showed that considering a subsonic turbulence with power peaking at 50 or 130 kpc, beam depolarization is strong up to a physical resolution of 10-20 kpc (with the average polarization decreasing from 35 – 65 % to 10 – 40 % at 1.5 GHz), while the average fractional polarization remains almost constant at larger resolution beams. Within our double radio relic sample only Abell 3667 has observations that resolve the 20 kpc scale (de Gasperin et al. 2022). We thus confirm that only a moderate decreasing trend of polarization fraction with resolution is observed for scales larger than  $\sim 30$  kpc. This is consistent with the simulations of Domínguez-Fernández et al. (2021), who considered a turbulent ICM with magnetic field strength of  $\sim 1\mu\text{G}$  within the relics.

The depolarization effect of external Faraday dispersion depends on the observing wavelength and on the RM dispersion experienced by the polarized emission (Burn 1966):

$$p(\lambda) = p_0 e^{-2\sigma_{\text{RM}}^2 \lambda^4}, \quad (10)$$

where  $p_0$  is the intrinsic polarization fraction at zero wavelength. We can use the RM dispersion computed for the radio

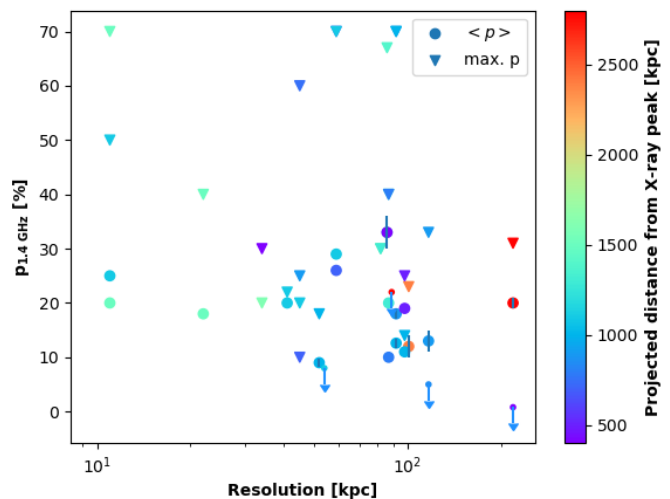


**Fig. 11.** Fractional polarization versus physical resolution of the observation for double radio relics. Each marker represents a single relic. Circles are average fractional polarization computed integrating over the polarized regions of the relic, downward triangles are the maximum values (therefore one relic can have both measurements in the plot). Arrows are upper limits computed for relics where we did not detect polarization. The color-scale represents the projected distance of the relic from the X-ray peak of the hosting galaxy cluster.

relics in this work to verify if external Faraday dispersion is able to account for the observed values of fractional polarization.

In the case of the western relic of 8C0212 we measured  $\sigma_{\text{RM}} = 10 \text{ rad m}^{-2}$ , i.e.  $14 \text{ rad m}^{-2}$  in its rest-frame. Considering an intrinsic  $p_0 = 62\%$  (computed with  $M = 3.2$  from Hoang et al. 2021) we would expect 33 % at 1.5 GHz using Eq. 10 for a perfectly edge-on relic, while we measured a maximum fractional polarization of 23 %. However, this relic is not very bright and we detected polarization only from the brightest regions while in others the upper limit on the fractional polar-

**Table 4.** Compilation of double radio relic galaxy clusters. Column 1: name of the cluster. A subscript letter specifies the relic; Column 2: redshift,  $z$ , retrieved from NED with the exception of 8C 0212+703 for which an updated redshift is provided by Zhang et al. (2020), and Abell 2146 for which the most updated redshift is in White et al. (2015); Column 3: average fractional polarization at 1.4 GHz; Column 4: maximum fractional polarization at 1.4 GHz; Column 5: median or average residual RM, already corrected for the Galactic contribution and for cosmological effects; Column 6: rest-frame corrected RM dispersion. Except for the northern relic in CIZA J2242.8+5301, for which QU-fitting was used, this value is computed over the relic area. For some relics we listed the total range of measured RM values included in squared brackets since the  $\sigma_{\text{RM}}$  is not reported; Column 7: observing beam of polarization observations; Column 8: physical resolution of the polarization observations; Column 9: projected distance of the relic from the X-ray centroid of the hosting galaxy cluster; Column 10: references for polarization observations, as for the legend. From this double radio relics list we excluded Abell 548b (Feretti et al. 2006), CIZA J0107.7+5408 (Randall et al. 2016), MACS J0025.4-1222 (Riseley et al. 2017), SPT-CL J0245-5302 (Zheng et al. 2018), RXC J2351.0-1934 (Duchesne et al. 2021c), and MACS J0417.5-1154, MCXC J0232.2-4420, MCXC J0516.6-5430 (Knowles et al. 2022) for which the characterization as double radio relics is still uncertain.

Cluster <sub>relic</sub>	$z$	$\langle p \rangle_{1.4\text{GHz}}$ [%]	max. $p_{1.4\text{GHz}}$ [%]	RRM $(1+z)^2$ [rad m <sup>-2</sup> ]	$\sigma_{\text{RM}}(1+z)^2$ [rad m <sup>-2</sup> ]	Obs. Beam	Physical resolution [kpc]	d [Mpc]	References
8C 0212+703 <sub>E</sub> (CIG 0217+70) <sup>a</sup>	0.180	<22	—	—	—	29'' × 29''	89	2.5	tw
8C 0212+703 <sub>W</sub> (CIG 0217+70)	0.180	12±2	23	-10	14	33'' × 33''	101	2.4	tw
Abell 1240 <sub>N</sub>	0.195	26	70	—	—	18'' × 18''	59	0.7	Bo09
Abell 1240 <sub>S</sub>	0.195	29	70	—	—	18'' × 18''	59	1.1	Bo09
Abell 2146 <sub>N</sub>	0.232	—	—	—	—	—	—	0.45	—
Abell 2146 <sub>S</sub>	0.232	—	—	—	—	—	—	0.2	—
Abell 2345 <sub>E</sub>	0.176	18±1	70	-0.3	8	30.5'' × 30.5''	92	0.9	S21
Abell 2345 <sub>W</sub>	0.176	12.6±0.9	70	-7	18	30.5'' × 30.5''	92	1.0	S21
Abell 3186 <sub>NW</sub> (MCXC J0352.4-7401)	0.127	—	—	—	—	—	—	1.5	—
Abell 3186 <sub>SE</sub> (MCXC J0352.4-7401)	0.127	—	—	—	—	—	—	1.2	—
Abell 3365 <sub>E</sub>	0.093	9.0±0.8	18	-13	13	30'' × 30''	52	1.0	tw
Abell 3365 <sub>W</sub>	0.093	<8	—	—	—	31'' × 31''	54	1.0	tw
Abell 3376 <sub>E</sub>	0.046	—	30	—	—	37'' × 25''	34	0.4	Ka12
Abell 3376 <sub>W</sub>	0.046	—	20	—	—	38'' × 26''	34	1.6	Ka12
Abell 3667 <sub>NW</sub>	0.055	20	70	—	[0-11]	10'' × 10''	11	1.5	dG22
Abell 3667 <sub>SE</sub>	0.055	25	50	—	[0-44]	10'' × 10''	11	1.1	dG22
Abell 521 <sub>NW</sub>	0.247	—	—	—	—	—	—	1.0	—
Abell 521 <sub>SE</sub>	0.247	—	—	—	—	—	—	0.75	—
ACT-CL J0102-4915 <sub>NW</sub> (El Gordo) <sup>b</sup>	0.87	33±1	67	38	21	11'' × 11''	86	1.4	Li14
ACT-CL J0102-4915 <sub>E</sub> (El Gordo) <sup>b</sup>	0.87	33±3	—	—	—	11'' × 11''	86	0.4	Li14
CIZA J2242.8+5301 <sub>N</sub> (Sausage)	0.189	18	40	-86 <sup>c</sup>	31	7'' × 7''	22	1.5	DG21
CIZA J2242.8+5301 <sub>S</sub> (Sausage)	0.189	20	22	—	[-14-0]	13'' × 13''	41	1.1	DG21
MACS J1752.0+4440 <sub>NE</sub>	0.366	20	40	—	—	17'' × 12''	87	1.3	Bo12
MACS J1752.0+4440 <sub>SW</sub>	0.366	10	40	—	—	17'' × 12''	87	0.8	Bo12
PLCK G200.9-28.2 <sub>NE</sub>	0.22	—	—	—	—	—	—	0.6	—
PLCK G200.9-28.2 <sub>SW</sub>	0.22	—	—	—	—	—	—	0.9	—
PLCK G287.0+32.9 <sub>N</sub> (PSZ2 G286.98+32.90)	0.39	<0.8	—	—	—	41'' × 41''	219	0.4	tw
PLCK G287.0+32.9 <sub>S</sub> (PSZ2 G286.98+32.90)	0.39	20±1	31	10	15	41'' × 41''	219	2.8	tw
PSZ1 G096.89+24.17 <sub>N</sub> (ZwCl 1856.8+6616)	0.304	—	60	—	—	10'' × 9''	45	0.75	J21
PSZ1 G096.89+24.17 <sub>S</sub> (ZwCl 1856.8+6616)	0.304	—	20	—	—	10'' × 9''	45	1.1	J21
PSZ1 G108.18-11.53 <sub>NE</sub>	0.335	—	30	—	—	17'' × 13''	82	1.7	dG15
PSZ1 G108.18-11.53 <sub>SW</sub>	0.335	—	30	—	—	17'' × 13''	82	1.3	dG15
PSZ2 G233.68+36.14 <sub>N</sub>	0.345	—	—	—	—	—	—	0.7	—
PSZ2 G233.68+36.14 <sub>SE</sub>	0.345	—	—	—	—	—	—	1.0	—
RXC J1314.4-2515 <sub>E</sub>	0.247	11	14	-5	17	25'' × 25''	98	1.0	S19
RXC J1314.4-2515 <sub>W</sub>	0.247	19	25	-11	17	25'' × 25''	98	0.5	S19
SPT-CL J2032-5627 <sub>NW</sub>	0.284	—	—	—	—	—	—	1.2	—
SPT-CL J2032-5627 <sub>SE</sub>	0.284	—	—	—	—	—	—	0.4	—
ZwCl 0008.8+5215 <sub>E</sub>	0.104	—	25	—	—	23.5'' × 17.0''	45	0.9	vW11
ZwCl 0008.8+5215 <sub>W</sub>	0.104	—	10	—	—	23.5'' × 17.0''	45	0.7	vW11
ZwCl 1447.2+2619 <sub>N</sub>	0.372	—	—	—	—	—	—	0.5	—
ZwCl 1447.2+2619 <sub>S</sub>	0.372	—	—	—	—	—	—	0.8	—
ZwCl 2341.1+0000 <sub>N</sub>	0.270	< 5	—	—	—	28'' × 28''	117	0.8	tw
ZwCl 2341.1+0000 <sub>S</sub>	0.270	13 ± 2	33	-3	35	28'' × 28''	117	0.9	tw

<sup>a</sup> We listed only the values obtained for source F in the eastern relic of 8C0212.

<sup>b</sup> The only available polarization and Faraday rotation study of this cluster was performed at 2.1 GHz.

<sup>c</sup> This value is computed as the median RM value subtracted by the median GRM estimated by Di Gennaro et al. (2021), although the authors noticed that this cluster is in a region heavily affected by the Galactic foreground and that the GRM could be underestimated.

**References legend:** tw this work, Bo09 Bonafede et al. (2009), S21 Stuardi et al. (2021), Ka12 Kale et al. (2012), dG22 de Gasperin et al. (2022), Li14 Lindner et al. (2014), DG21 Di Gennaro et al. (2021), Bo12 Bonafede et al. (2012), J21 Jones et al. (2021), dG15 de Gasperin et al. (2015), S19 Stuardi et al. (2019), vW11 van Weeren et al. (2011b).

ization reaches the 30 %. Therefore, our measurements are in agreement with external depolarization. We do not have information about the ICM distribution at the position of the relics in 8C0212. New X-ray and optical observation are necessary in order to understand the environment of this radio relic, the dynamic that led to its formation and possible projection effects that could further contribute to its depolarization.

The same calculation can be repeated for the eastern radio relic of A3365. We measured  $\sigma_{\text{RM}} = 11 \text{ rad m}^{-2}$  ( $13 \text{ rad m}^{-2}$  in

the source rest-frame) and a maximum  $p$  of 18 %. Upper limits in non-detected regions also do not exceed the 20 % level. However, in this case an underlying shock wave with Mach number 3.5 was detected with X-ray observations Urdampilleta et al. (2021). Thus, projection effects cannot be the origin of such low fractional polarization. One possibility is that we are detecting polarization only from the external layer of the radio relic, while the RM dispersion is much larger within it. We therefore suggest that internal Faraday dispersion is present with



**Table 5.** Spectral index and Mach number estimates for our compilation of double radio relic galaxy clusters. Column 1: name of the cluster. A subscript letter specifies the relic; Column 2: injection spectral index. Column 3: radio injection Mach number retrieved from the literature (Eq. 14); Column 4: integrated spectral index; Column 5: radio Mach number derived from the integrated spectral index using Eq. 13. We used the \*\* symbol for  $\alpha_{\text{int}} \leq 1$  since it is incompatible with DSA predictions.  $1\sigma$  uncertainties are derived with standard propagation; Column 6: references for injection spectral index and Mach number and for integrated spectral index, as for the legend. For Abell 521<sub>NW</sub> and PLCK G200.9-28.2<sub>NE</sub> we give the reference for the discovery but no spectral index is available.

Cluster <sub>relic</sub>	$\alpha_{\text{inj}}$	$M_{\text{inj}}$	$\alpha_{\text{int}}$	$M_{\text{int}}$	References
8C 0212+703 <sub>E</sub> (CIG 0217+70)	0.93±0.08	2.4±0.2	1.09±0.06	5±1	H21
8C 0212+703 <sub>W</sub> (CIG 0217+70)	0.72±0.05	3.2 <sup>+0.4</sup> <sub>-0.3</sub>	1.01±0.05	**	H21
Abell 1240 <sub>N</sub>	0.94±0.06	2.4±0.1	1.08±0.05	5±1	H18
Abell 1240 <sub>S</sub>	0.97±0.05	2.3±0.1	1.13±0.05	4.0±0.7	H18
Abell 2146 <sub>N</sub>	1.06±0.09	2.1±0.1	1.14±0.08	4±1	H19
Abell 2146 <sub>S</sub>	1.13±0.06	2.0±0.1	1.25±0.07	3.0±0.4	H19
Abell 2345 <sub>E</sub>	–	–	1.29±0.07	2.8±0.3	Ge17
Abell 2345 <sub>W</sub>	–	–	1.52±0.08	2.2±0.1	Ge17
Abell 3186 <sub>NW</sub> (MCXC J0352.4-7401)	–	–	1±0.1	**	D21c
Abell 3186 <sub>SE</sub> (MCXC J0352.4-7401)	–	–	0.9±0.1	**	D21c
Abell 3365 <sub>E</sub>	–	–	0.85±0.03	**	D21c
Abell 3365 <sub>W</sub>	–	–	0.76±0.08	**	D21c
Abell 3376 <sub>E</sub>	0.70±0.15	3.3±0.3	1.33±0.08	2.7±0.3	Ka12, C22
Abell 3376 <sub>W</sub>	1.0±0.2	2.2±0.4	1.22±0.05	3.2±0.3	Ka12, C22
Abell 3667 <sub>NW</sub>	1.0±0.1	2.2 <sup>+0.2</sup> <sub>-0.1</sub>	1.13±0.02	4.0±0.3	dG22
Abell 3667 <sub>SE</sub>	–	–	0.93±0.03	**	dG22
Abell 521 <sub>NW</sub>	–	–	–	–	Kn22
Abell 521 <sub>SE</sub>	–	–	1.48±0.01	2.27±0.02	Gi08
ACT-CL J0102-4915 <sub>NW</sub> (El Gordo)	0.86±0.15	2.5 <sup>+0.7</sup> <sub>-0.3</sub>	1.25±0.04	3.0±0.2	Li14, tw
ACT-CL J0102-4915 <sub>E</sub> (El Gordo)	–	–	1.06±0.04	6±2	Li14, tw
CIZA J2242.8+5301 <sub>N</sub> (Sausage)	0.86±0.05	2.6±0.2	1.12±0.03	4.2±0.5	DG18, Lo20
CIZA J2242.8+5301 <sub>S</sub> (Sausage)	1.09±0.05	2.10±0.08	1.12±0.07	4±1	DG18
MACS J1752.0+4440 <sub>NE</sub>	0.6	4.6	1.16±0.03	3.7±0.3	Bo12, vW12
MACS J1752.0+4440 <sub>SW</sub>	0.8	2.8	1.10±0.05	5±1	Bo12, vW12
PLCK G200.9-28.2 <sub>NE</sub>	–	–	–	–	Kn22
PLCK G200.9-28.2 <sub>SW</sub>	0.7±0.2	3±2	1.21±0.15	3±1	Ka17
PLCK G287.0+32.9 <sub>N</sub> (PSZ2 G286.98+32.90)	–	–	1.19±0.03	3.4±0.2	Ge17
PLCK G287.0+32.9 <sub>S</sub> (PSZ2 G286.98+32.90)	–	–	1.36±0.04	2.6±0.1	Ge17
PSZ1 G096.89+24.17 <sub>N</sub> (ZwCl 1856.8+6616)	0.87±0.07	2.5±0.2	0.92±0.04	**	J21, tw
PSZ1 G096.89+24.17 <sub>S</sub> (ZwCl 1856.8+6616)	0.97±0.07	2.3±0.2	1.14±0.03	3.6±0.4	J21, tw
PSZ1 G108.18-11.53 <sub>NE</sub>	1.02 <sup>+0.04</sup> <sub>-0.08</sub>	2.20 <sup>+0.07</sup> <sub>-0.14</sub>	1.25±0.02	3.0±0.1	dG15
PSZ1 G108.18-11.53 <sub>SW</sub>	0.952 <sup>+0.09</sup> <sub>-0.12</sub>	2.3 <sup>+0.2</sup> <sub>-0.3</sub>	1.28±0.02	2.85±0.09	dG15
PSZ2 G233.68+36.14 <sub>N</sub>	1.07±0.11	2.1 <sup>+0.2</sup> <sub>-0.1</sub>	1.31±0.12	2.7±0.5	Gh21
PSZ2 G233.68+36.14 <sub>SE</sub>	0.67±0.11	3.5 <sup>+2.3</sup> <sub>-0.7</sub>	0.97±0.13	**	Gh21
RXC J1314.4-2515 <sub>E</sub>	–	–	1.2±0.2	3±1	S19
RXC J1314.4-2515 <sub>W</sub>	–	–	1.5±0.1	2.2±0.2	S19
SPT-CL J2032-5627 <sub>NW</sub>	–	–	1.2±0.1	3.3 ± 0.7	D21a
SPT-CL J2032-5627 <sub>SE</sub>	–	–	1.5±0.1	2.2 ± 0.2	D21a
ZwCl 0008.8+5215 <sub>E</sub>	1.2±0.2	2.2 <sup>+0.2</sup> <sub>-0.1</sub>	1.59±0.06	2.09±0.08	vW11
ZwCl 0008.8+5215 <sub>W</sub>	1.0±0.15	2.4 <sup>+0.4</sup> <sub>-0.2</sub>	1.49±0.12	2.2±0.2	vW11
ZwCl 1447.2+2619 <sub>N</sub>	–	–	1.27±0.31	3 ± 1	Le22
ZwCl 1447.2+2619 <sub>S</sub>	–	–	1.68±0.3	2.0 ± 0.3	Le22
ZwCl 2341.1+0000 <sub>N</sub>	–	2.4 ± 0.4	1.02±0.02	**	Z21, tw
ZwCl 2341.1+0000 <sub>S</sub>	1.00±0.06	2.2 ± 0.1	0.98±0.02	**	Z21, tw

**References legend:** tw this work, H21 Hoang et al. (2021), H18 Hoang et al. (2018), H19 Hoang et al. (2019), Ge17 George et al. (2017), D21c Duchesne et al. (2021a), Ka12 Kale et al. (2012), C22 Chibueze et al. (2022), dG22 de Gasperin et al. (2022), Kn22 Knowles et al. (2022), Gi08 Giacintucci et al. (2008), Li14 Lindner et al. (2014), DG18 Di Gennaro et al. (2018), Lo20 Loi et al. (2020), Bo12 Bonafede et al. (2012), vW12 (van Weeren et al. 2012), Ka17 Kale et al. (2017), J21 Jones et al. (2021), dG15 de Gasperin et al. (2015), Gh21 Ghirardini et al. (2021), S19 Stuardi et al. (2019), D21a Duchesne et al. (2021b), vW11 van Weeren et al. (2011b), Le22 Lee et al. (2022), Z21 Zhang et al. (2021).

$\sigma_{\text{RM}} < 45 \text{ rad m}^{-2}$ , i.e. with an RM dispersion lower than our

resolution in Faraday space. Using the formula for internal Faraday dispersion provided by Arshakian & Beck (2011):

$$p(\lambda) = p_0 \frac{1 - e^{-2\sigma_{\text{RM}}^2 \lambda^4}}{2\sigma_{\text{RM}}^2 \lambda^4}, \quad (11)$$

we obtain that  $\sigma_{\text{RM}} \sim 30 \text{ rad m}^{-2}$  is sufficient to reduce the fractional polarization to the observed value. This value is consistent with internal RM dispersion found in MHD simulations of radio relics (Domínguez-Fernández et al. 2021, see also Sec. 4.3).

The Faraday depolarization, internal and/or external, could also explain the non-detection in polarization of the bright northern relic in the PLCK287 galaxy cluster. An external  $\sigma_{\text{RM}} \geq 30 \text{ rad m}^{-2}$  or an internal  $\sigma_{\text{RM}} \geq 155 \text{ rad m}^{-2}$  or a combination of the two are able to completely depolarize the signal below the 0.8 % level at 1.5 GHz. In this case, the position of the radio relic nearby the galaxy cluster center can clearly account for such level of RM dispersion.

An RM dispersion of  $\sigma_{\text{RM}} = 22 \text{ rad m}^{-2}$  ( $35 \text{ rad m}^{-2}$  at the cluster's redshift) as we found for the southern relic of ZwCl2341 is able to explain the low fractional polarization observed for this relic. Moreover, projection effects are likely to lower the polarization fraction of the relics in this system, as also suggested by their non arc-like shape and from the complex X-ray structure of the system (Zhang et al. 2021).

In conclusion, at the physical resolution of current observations (i.e.,  $> 30 \text{ kpc}$ ) the fractional polarization level of radio relics is already heavily dominated by beam-independent depolarization effects at 1.4 GHz. Both external and internal Faraday depolarization contribute to their observed polarization fraction. This is consistent with simulations in which a tangled magnetic field of strength  $\sim 1 \mu\text{G}$  is compressed by a shock wave propagating in a turbulent ICM (Domínguez-Fernández et al. 2021).

#### 4.2. Fractional polarization and Mach number

The fractional polarization of radio relics is expected to increase with higher shock Mach numbers. Using again the analytical expression derived by Ensslin et al. (1998) for an edge-on relic, the average fractional polarization is expected to increase from 41 % up to 62 % going from  $M = 1.5$  to  $M = 3$ . A much smoother increase is expected for Mach numbers higher than 3, with  $\langle p \rangle = 64 \%$  for  $M = 4.5$ . A similar trend is obtained by more complex semi-analytical models which also considered the dependence on magnetic field strength (Hoeft et al. 2022).

The shock Mach number can be derived from the spectral index of the radio emission assuming particle acceleration via DSA (e.g., Colafrancesco et al. 2017), or from the surface brightness and temperature jump measured from X-ray images (e.g., Akamatsu & Kawahara 2013). The long-standing problem of the discrepancy between radio- and X-ray-derived Mach numbers (with the radio Mach number being generally higher), recently found a plausible explanation discussed in Wittor et al. (2021). Based on the numerical view of simulated shocks, it is reasonable that rather than a single uniform Mach number, radio relics are characterized by a Mach number distribution which depends on the initial strength of the shock wave and on the turbulent fluctuations in the upstream ICM (Skillman et al. 2013; Domínguez-Fernández et al. 2021). While radio observations are more sensitive to the highest Mach numbers within the distribution, which produce the highest radio emissivity, X-ray measurements reflect the average of the distribution (e.g., Hong et al. 2015; Wittor et al. 2021). Furthermore, X-ray measurements are heavily affected by radio relic's orientation and are biased towards lower values in the case of inclination with respect to the line of sight. For this reason, Wittor et al. (2021) concluded that Mach numbers derived from the integrated spectral indexes are more robust.

However in this case, beside the DSA mechanism, a further assumption of planar and stationary shock condition has to be made in order to derive  $M$ . Under these assumptions the integrated spectral index,  $\alpha_{\text{int}}$ , is related to the injection spectral index,  $\alpha_{\text{inj}}$ , by the simple relation

$$\alpha_{\text{int}} = \alpha_{\text{inj}} + 0.5, \quad (12)$$

and the Mach number is:

$$M_{\text{int}} = \sqrt{\frac{\alpha_{\text{int}} + 1}{\alpha_{\text{int}} - 1}}, \quad (13)$$

where  $\alpha_{\text{int}} > 1$ . Alternatively, the radio Mach number can be derived from the injection spectral index measured at the shock front from spatially resolved spectral index maps. In this case

$$M_{\text{inj}} = \sqrt{\frac{2\alpha_{\text{inj}} + 3}{2\alpha_{\text{inj}} - 1}}. \quad (14)$$

While Mach numbers derived from the integrated spectral index can be biased due to simplified assumptions (e.g., Kang 2015) and inaccurate source-subtraction, the estimates derived from the injection spectral index can be biased by coarse spatial resolution, projection effects and misalignment between the radio images.

For the 22 double relic systems, in Tab. 5 we listed both the Mach number derived from the injection spectral index measured from resolved spectral index maps found in the literature, and the Mach number that we computed with Eq. 13 using the integrated spectral index values (also listed in the table). In the latter case, we notice that the simple DSA with stationary assumption cannot be applied to 10 radio relics within our sample since they have  $\alpha_{\text{int}} \leq 1$ . This disagreement with the DSA theory may be partially ascribed to the underestimation of the uncertainties on spectral index estimates which, as discussed earlier, can be biased for a number of reasons.

For some of the relics, we computed the integrated spectral index using archival and/or proprietary broad-band observations in order to reduce the uncertainty on the derived Mach number. Flux densities and updated spectral index estimates, together with the plots of the spectra, are reported in the Appendix A.

We also notice that often  $M_{\text{inj}} < M_{\text{int}}$ , with the majority of  $M_{\text{inj}}$  being lower than 3. While the injection Mach number show significant variation across the relic, the integrated Mach number is based on the emission-weighted spectral index where higher Mach numbers have more weight. Therefore, the average injection Mach number is often lower than the integrated one. However, with accurate and highly-resolved spectral index maps it is possible to consistently recover the injection and the integrated Mach numbers (see e.g., Rajpurohit et al. 2018).

We searched for a correlation between fractional polarization (or maximum fractional polarization value) and Mach number. Plots are shown in Fig. 12. We found very weak correlations both between fractional polarization and the Mach number estimated from the injection index (Spearman correlation coefficients -0.23 for  $\langle p \rangle$  and 0.22 for the maximum  $p$ ) and with the Mach number estimated from the integrated radio spectrum (Spearman correlation coefficients 0.29 and 0.24 for  $\langle p \rangle$  and the maximum  $p$ , respectively). The weak correlation can be partially due to the large uncertainties on Mach number estimates and on

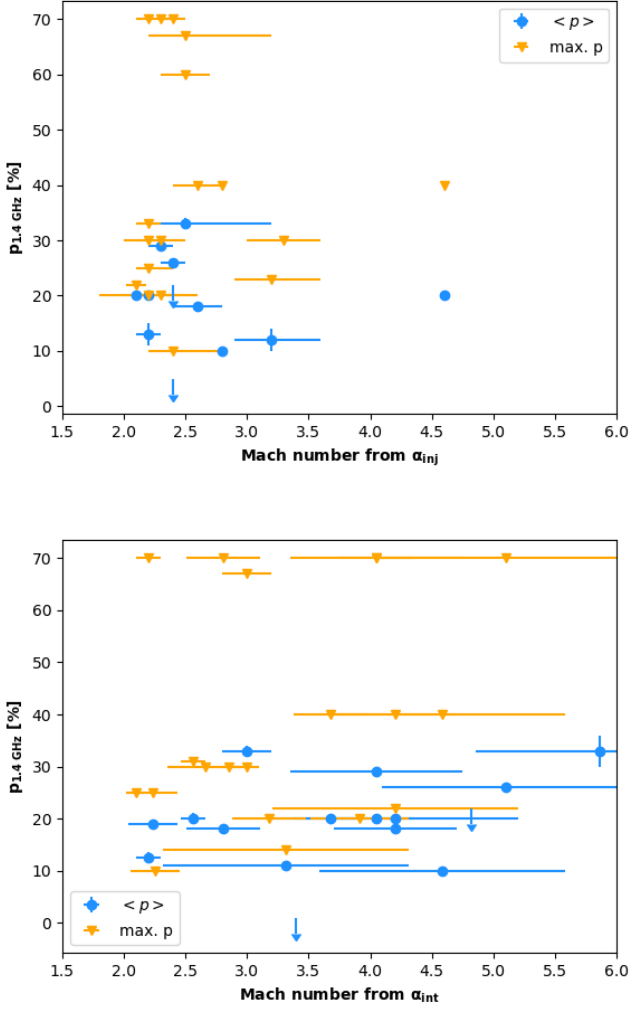


**Fig. 12.** Fractional polarization versus Mach number obtained from the injection spectral index (upper panel) and from the integrated spectral index (bottom panel). Each marker represents a single relic. Blue circles are average fractional polarization computed integrating over the polarized regions of the relic, orange downwards triangles are the maximum values (therefore one relic can have both measurements in the plot). Arrows are upper limits computed for relics where we did not detect polarization.

the aforementioned possible bias present in both methods. However, the Spearman correlation coefficient is positive for both  $\langle p \rangle$  and the maximum  $p$  only for the integrated Mach number, and it reaches the highest value in the correlation between  $M_{int}$  and  $\langle p \rangle$ . We interpret this fact as a suggestion that the Mach number estimated from the integrated spectral index is in fact more robust, as suggested by Wittor et al. (2019).

Furthermore, while the majority of injection-derived Mach numbers are lower than 3, the distribution of  $M_{int}$  is shifted towards higher values where we expect a weaker correlation between fractional polarization and Mach number (see Fig. 1 in Hoeft et al. 2022). If the Mach number distribution would be the one described by  $M_{inj}$  we would have found a stronger correlation. This suggests that the bulk of double radio relics reaches maximum Mach numbers  $M > 2.5 - 3$ , as required by particle acceleration models from the thermal pool which would require

an unrealistically high acceleration efficiency for  $M \leq 2$  (Botteon et al. 2020; Domínguez-Fernández et al. 2021). Also the fractional polarization observed in radio relics would be difficult to reproduce with  $M \leq 2$  due to the low level of magnetic field compression (Domínguez-Fernández et al. 2021).

Overall, the observed weak positive trend of fractional polarization with Mach number can be explained in the context of turbulent magnetic field compression for  $M > 2.5 - 3$ . The magnetic field strength has also a major role in determining the fractional polarization level of radio relics due to its impact on particle aging (Hoeft et al. 2022).

#### 4.3. Faraday rotation properties

The average (or median) residual RM of double radio relics in the cluster's rest-frame spans between  $-13 \text{ rad m}^{-2}$  and  $38 \text{ rad m}^{-2}$ , with the only exception of CIZA J2242.8+5301 ( $-86 \text{ rad m}^{-2}$ ) for which an high residual contribution from the Galactic RM is very likely (Di Gennaro et al. 2021). The measured RRM are in the lower range of relics RMs predicted by MHD cosmological simulations which only take into account the external ICM contribution and spans in the range  $10\text{--}100 \text{ rad m}^{-2}$  (Wittor et al. 2019). This is consistent with double radio relics being seen edge-on and lying in the outskirts of galaxy clusters, therefore crossing a small Faraday-rotating volume.

The rest-frame RM dispersion spans between  $8 \text{ rad m}^{-2}$  and  $35 \text{ rad m}^{-2}$ , perfectly consistent with MHD cosmological simulations which predict  $\sigma_{RM}$  of few tens for edge-on relics and  $\sigma_{RM}$  of few hundreds for face-on relics (Wittor et al. 2019). However, due to external Faraday dispersion,  $\sigma_{RM}$  larger than  $40 \text{ rad m}^{-2}$  would be undetectable at  $1.5 \text{ GHz}$ , because the signal would be totally depolarized. Higher-frequency observations are needed to exclude a possible observing bias.

Domínguez-Fernández et al. (2021) simulated the internal RM of radio relic within a  $(200 \text{ kpc})^3$  volume. They found that the RM dispersion within relics depends on the pre-shock turbulent conditions of the ICM. In particular, they found that a subsonic turbulence with power peaking at larger scales produces a higher internal RM dispersion as a consequence of a broader magnetic field distribution. They also found that the internal RM distribution tends to narrow when taking into account only brighter radio emitting regions, as expected for polarization measurements.

We did not detect internal Faraday rotation with RM dispersion larger than  $45 \text{ rad m}^{-2}$  in our four galaxy clusters. We infer the presence of internal Faraday rotation with  $\sigma_{RM} \sim 30 \text{ rad m}^{-2}$  in the eastern relic of A3365 due to its strong depolarization. The only double radio relic with internal Faraday rotation detected in the literature is the western radio relic of RXC J1314.4-2515 which shows an internal RM dispersion of  $\sim 100 \text{ rad m}^{-2}$  (Stuardi et al. 2019). An internal RM dispersion lower than  $100 \text{ rad m}^{-2}$  is line with simulations which account for a pre-shock turbulence with power peaking at  $\sim 50 \text{ kpc}$  while larger scale turbulence would imply larger internal RM dispersion (see Fig. 16 Domínguez-Fernández et al. 2021). In these simulations the magnetic field strength is  $1.5 \mu\text{G}$ .

Both Wittor et al. (2019) and Domínguez-Fernández et al. (2021) found an asymmetric and non-Gaussian RM distribution in radio relics. This was previously noticed by Vazza et al. (2018), who analyzed highly resolved MHD simulations of entire galaxy clusters. They noticed that the non-Gaussian behavior increases with the simulation resolution and with distance from the cluster center. This resulted in higher RMs values with respect to a Gaussian distribution that could affect the magnetic

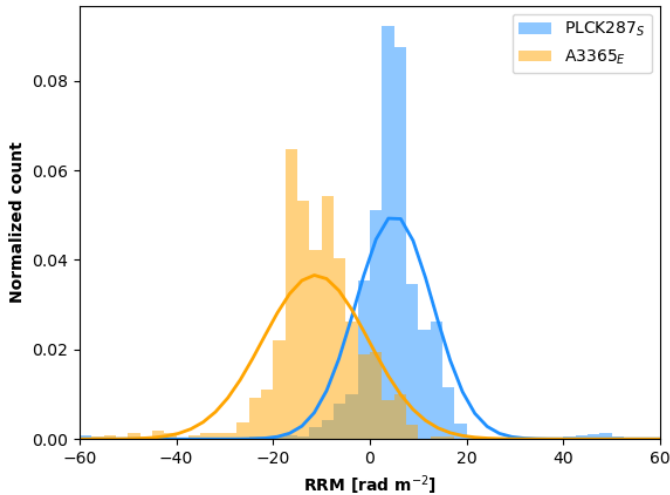


**Fig. 13.** Normalized Residual Rotation Measure distributions (in the observer rest-frame) of the eastern relic of A3365 (orange) and of the southern relic of PLCK287 (blue). The two distributions are compared with Gaussian distributions having the same mean and standard deviation (blue and orange lines)

field estimate derived from RM modeling. We show the RM distributions of the southern relic of PLCK287 and the eastern relic of A3365 compared to their fit with a Gaussian distributions in Fig. 13. Both RRM distributions are non-Gaussian, similarly to what is found in other double radio relics (Stuardi et al. 2019, 2021; Di Gennaro et al. 2021). The distribution of RMs is also non-symmetric for Abell 3365. Compared to Gaussian distributions, the observed ones are more peaked and skewed to higher RMs. A similar result was also found by Vazza et al. (2018).

In Fig. 14 we show the fractional polarization of double relics at 1.4 GHz as a function of intrinsic RM and  $\sigma_{RM}$ . We did not find significant correlation between the considered quantities. This confirms that different depolarization effects (differential Faraday rotation, internal and external Faraday dispersion) together contribute to the final fractional polarization observed at 1.4 GHz.

We observed a very good alignment of magnetic field line direction with the main axis of the southern radio relic of PLCK287 on Mpc-scales (see Fig. 7). The alignment is less clear for the eastern relic in A3365 (Fig. 5). MHD simulations are able to reproduce the magnetic field alignment with the shock front for edge-on relics but only on small scales, i.e.  $\leq 200$  kpc (Skillman et al. 2013; Wittor et al. 2019). Domínguez-Fernández et al. (2021) showed that the magnetic field alignment can increase with decreasing resolution of the radio observation since larger resolution elements weight more the brightest regions where the polarization vector is aligned with the shock normal. We notice that PLCK287 is the cluster for which we have the lowest physical resolution. The fact that many radio relics show ordered magnetic field lines on Mpc-scale agrees with our finding that the physical resolution of current observations ( $> 30$  kpc) is not strongly affecting their fractional polarization properties (Sec. 4.1). The turbulent scales causing depolarization and magnetic field misalignment are already resolved-out above 20 kpc and we can only observe the brightest regions where magnetic field vectors are aligned. However, simulations show that the level of magnetic field alignment depends also on the phys-

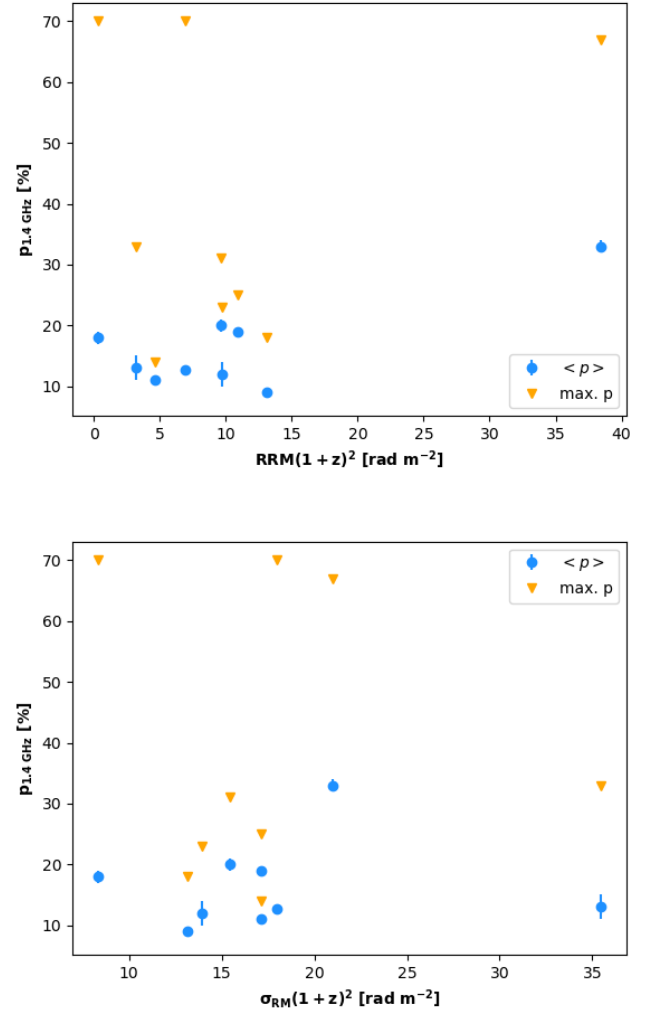


**Fig. 14.** Fractional polarization versus intrinsic residual RM (RRM, i.e. corrected for Galactic contribution and cosmological shift, upper panel) and intrinsic RM dispersion (bottom panel). Blue circles are average fractional polarization computed by integrating over the polarized regions of the relic, orange downwards triangles are the maximum values (therefore one relic can have both measurements in the plot).

ical scale of the upstream turbulence, therefore the differences that we observed between radio relics could also reflect different physical conditions of the ICM.

## 5. Conclusions

In this paper we produced and analyzed polarization and Faraday rotation images of four famous double radio relics galaxy clusters in the 1-2 GHz frequency range using JVLA observations. For our polarization analysis we used RM synthesis (Brentjens & de Bruyn 2005). With this work we almost doubled the number of double radio relics with available Faraday rotation information. Among our sample, we detected extended polarized emission only from two relics, while the remaining relics are either totally depolarized at 1.5 GHz, or show only few patches of polarized emission. We focused on the possible origin of depolarization. In particular:

- **8C 0212+703 (CIG 0217+70)**. In the 8C0212 galaxy cluster we detected a maximum fractional polarization of 23 % from the western radio relic (source C) confirming its identification as a radio relic (Hoang et al. 2021). We also detected polarization from the lobes of the radio galaxy close to the eastern radio relic (source E1) while the other parts of the relic (sources D, F and G) are undetected in polarization with 28 % upper limit to the fractional polarization.
- **Abell 3365**. We detected a low level of fractional polarization (i.e., < 18 %) and only from the eastern radio relic. Since the external RM dispersion measured is low (13 rad m<sup>-2</sup> in the source rest-frame) we suggest that a possible cause of depolarization is internal Faraday dispersion with  $\sigma_{\text{RM}} \sim 30$  rad m<sup>-2</sup>. Magnetic field vectors are not aligned with the main axis of the relic along the whole relic extent.
- **PLCK G287.0+32.9 (PSZ2 G286.98+32.90)**. Only the southern relic of PLCK287 is detected in polarization with  $p > 20 \pm 1$  %, and the magnetic field vectors are well aligned with its main axis. Notably, also the faint upstream extension of the relic is polarized. The northern relic is likely depolarized at 1.5 GHz, due its proximity to the cluster center (Bonafede et al. 2014). The connection of the northern relic with the large radio galaxy in the north-east is supported by the similarity of its RM properties and the one of the closest cluster galaxy.
- **ZwCl 2341.1+0000**. The northern relic of ZwCl2341 is unpolarized, with fractional polarization upper limit of 5%. This is consistent with previous 2-4 GHz observations (Benson et al. 2017). We concluded that previous low-resolution 1.4 GHz observations that found higher fractional polarization values were contaminated by the nearby head-tail radio galaxy (Giovannini et al. 2010). The southern relic shows few patches of polarized emission with  $p > 13 \pm 2$  %. Projection effects are likely to play an important role in the depolarization of these relics, as suggested by the disturbed X-ray morphology of the cluster (Zhang et al. 2021), merger components along the line-of-sight (Golovich et al. 2019b) and high  $\sigma_{\text{RM}}$  value (i.e., 35 rad m<sup>-2</sup> in the source rest-frame).

In order to place our results into a broader context, we made an updated compilation of all double radio relics known to date and we statistically analyzed their polarization and Faraday rotation properties at 1.4 GHz. We listed 22 double radio relics: 15 have polarization information. These are our main conclusions:

- almost all radio double radio relics in the literature have been observed with physical resolution coarser than 30 kpc. In this resolution range, we found a moderate decreasing trend of the average fractional polarization of radio relics with the physical size of the observing beam. This is consistent with simulation suggesting the presence of turbulence with the physical scale peaking between 50 and 130 kpc in the upstream ICM which causes beam-dependent depolarization only up to  $\sim 20$  kpc (Domínguez-Fernández et al. 2021).
- Both external and internal Faraday dispersion contribute to the observed polarization fraction at 1.4 GHz. In particular, internal Faraday dispersion with  $\sigma_{\text{RM}} < 45$  rad m<sup>-2</sup> should be accounted for in order to explain the low fractional polarization of some double radio relics, since the detected external RM dispersion is not enough to depolarize them to the observed value.
- We found a weak positive correlation between the fractional polarization of relics and shock Mach number estimated

from the integrated spectrum of radio relics (Spearman coefficient  $\sim 0.3$ ). Such a weak correlation is expected for Mach numbers higher than 2.5, while for lower values a stronger correlation would be expected (Hoeft et al. 2022). This suggests that most radio relics reach a maximum Mach number higher than 2.5 and that Mach number estimates from X-ray or from injection radio spectral indexes are biased towards lower values. This founding would help explaining the origin of radio relics, since, with the standard DSA from the thermal pool, Mach numbers lower than 2.5 are not expected to generate the radio luminosity and the polarization fraction observed from radio relics (Botteon et al. 2020; Domínguez-Fernández et al. 2021; Domínguez-Fernández et al. 2021). However, we notice that the large uncertainties on Mach number estimates still prevent strong conclusions.

- Although the number of radio relics with available Faraday rotation information is still low, we found that the global RM properties of double radio relics are well reproduced by the state-of-the-art MHD simulations (Wittor et al. 2019). Both observed RM and  $\sigma_{\text{RM}}$  of double radio relics are consistent with what is expected from edge-on relics in cosmological MHD simulations. The amount of internal Faraday rotation observed from double radio relics can be explained by the presence of a turbulent ICM up-stream of the shocks with power peaking at  $\sim 50$  kpc scales and turbulent magnetic fields of strength  $\sim 1\mu\text{G}$ , as simulated by Domínguez-Fernández et al. (2021). We confirm that the RM distribution of radio relics is non-Gaussian and that magnetic field lines appear more aligned at lower resolution.

*Acknowledgements.* C.S. and A.B. acknowledge support from the MIUR grant FARE “SMS” and from the ERC-StG DRANOEL, n. 714245. F.V. acknowledges support from the ERC-StG MAGCOW, n. 714196. R.J.vW. acknowledges support from the ERC Starting Grant ClusterWeb n. 804208. We thank the anonymous referee for useful suggestions.

## References

- Abell, G. O. 1958, *ApJS*, 3, 211
- Akamatsu, H. & Kawahara, H. 2013, *Publications of the Astronomical Society of Japan*, 65, 16
- Arshakian, T. G. & Beck, R. 2011, *MNRAS*, 418, 2336
- Bagchi, J., Enßlin, T. A., Miniati, F., et al. 2002, *New A*, 7, 249
- Bagchi, J., Sankhyayan, S., Sarkar, P., et al. 2017, *ApJ*, 844, 25
- Bagchi, J., Sirothia, S. K., Werner, N., et al. 2011, *ApJ*, 736, L8
- Bennett, C. L., Larson, D., Weiland, J. L., & Hinshaw, G. 2014, *ApJ*, 794, 135
- Benson, B., Wittman, D. M., Golovich, N., et al. 2017, *ApJ*, 841, 7
- Bonafede, A., Brüggen, M., van Weeren, R., et al. 2012, *MNRAS*, 426, 40
- Bonafede, A., Cassano, R., Brüggen, M., et al. 2017, *MNRAS*, 470, 3465
- Bonafede, A., Giovannini, G., Feretti, L., Govoni, F., & Murgia, M. 2009, *A&A*, 494, 429
- Bonafede, A., Intema, H. T., Brüggen, M., et al. 2014, *ApJ*, 785, 1
- Bonafede, A., Vazza, F., Brüggen, M., et al. 2013, *MNRAS*, 433, 3208
- Boschin, W., Girardi, M., & Barrena, R. 2013, *MNRAS*, 434, 772
- Botteon, A., Brunetti, G., Ryu, D., & Roh, S. 2020, *A&A*, 634, A64
- Brentjens, M. A. & de Bruyn, A. G. 2005, *A&A*, 441, 1217
- Brown, S. & Rudnick, L. 2011, *MNRAS*, 412, 2
- Burn, B. J. 1966, *MNRAS*, 133, 67
- Caprioli, D. & Spitkovsky, A. 2014, *ApJ*, 783, 91
- Carretti, E., Vacca, V., O’Sullivan, S. P., et al. 2022, *MNRAS*, 512, 945
- Chibueze, J. O., Akamatsu, H., Parekh, V., et al. 2022, *PASJ*
- Colafrancesco, S., Marchegiani, P., & Paulo, C. M. 2017, *MNRAS*, 471, 4747
- Condon, J. J., Cotton, W. D., Greisen, E. W., et al. 1998, *AJ*, 115, 1693
- Cornwell, T. J., Golap, K., & Bhatnagar, S. 2008, *IEEE Journal of Selected Topics in Signal Processing*, 2, 647
- de Gasperin, F., Intema, H. T., van Weeren, R. J., et al. 2015, *MNRAS*, 453, 3483
- de Gasperin, F., Rudnick, L., Finoguenov, A., et al. 2022, *A&A*, 659, A146
- de Gasperin, F., van Weeren, R. J., Brüggen, M., et al. 2014, *MNRAS*, 444, 3130
- Delain, K. M. & Rudnick, L. 2006, *Astronomische Nachrichten*, 327, 561
- Di Gennaro, G., van Weeren, R. J., Hoeft, M., et al. 2018, *ApJ*, 865, 24
- Di Gennaro, G., van Weeren, R. J., Rudnick, L., et al. 2021, *ApJ*, 911, 3

- Dominguez-Fernandez, P., Brüggen, M., Vazza, F., et al. 2021, *MNRAS*, 500, 795
- Domínguez-Fernández, P., Brüggen, M., Vazza, F., et al. 2021, *MNRAS*, 507, 2714
- Donnert, J., Vazza, F., Brüggen, M., & ZuHone, J. 2018, *Space Sci. Rev.*, 214, 122
- Duchesne, S. W., Johnston-Hollitt, M., & Bartalucci, I. 2021a, *PASA*, 38, e053
- Duchesne, S. W., Johnston-Hollitt, M., Bartalucci, I., Hodgson, T., & Pratt, G. W. 2021b, *PASA*, 38, e005
- Duchesne, S. W., Johnston-Hollitt, M., Offringa, A. R., et al. 2021c, *PASA*, 38, e010
- Ensslin, T. A., Biermann, P. L., Klein, U., & Kohle, S. 1998, *A&A*, 332, 395
- Feretti, L., Bacchi, M., Slee, O. B., et al. 2006, *MNRAS*, 368, 544
- Finner, K., Jee, M. J., Golovich, N., et al. 2017, *ApJ*, 851, 46
- George, L. T., Dwarakanath, K. S., Johnston-Hollitt, M., et al. 2017, *MNRAS*, 467, 936
- George, S. J., Stil, J. M., & Keller, B. W. 2012, *Publications of the Astronomical Society of Australia*, 29, 214
- Ghirardini, V., Bulbul, E., Hoang, D. N., et al. 2021, *A&A*, 647, A4
- Giacintucci, S., Venturi, T., Macario, G., et al. 2008, *A&A*, 486, 347
- Giovannini, G., Bonafede, A., Feretti, L., Govoni, F., & Murgia, M. 2010, *A&A*, 511, L5
- Golovich, N., Dawson, W. A., Wittman, D. M., et al. 2019a, *The Astrophysical Journal Supplement Series*, 240, 39
- Golovich, N., Dawson, W. A., Wittman, D. M., et al. 2019b, *ApJ*, 882, 69
- Guo, X., Sironi, L., & Narayan, R. 2014a, *ApJ*, 794, 153
- Guo, X., Sironi, L., & Narayan, R. 2014b, *ApJ*, 797, 47
- Ha, J.-H., Ryu, D., & Kang, H. 2018, *ApJ*, 857, 26
- Hales, C. A., Gaensler, B. M., Norris, R. P., & Middelberg, E. 2012, *MNRAS*, 424, 2160
- Heald, G. 2009, in *IAU Symposium*, Vol. 259, *Cosmic Magnetic Fields: From Planets, to Stars and Galaxies*, ed. K. G. Strassmeier, A. G. Kosovichev, & J. E. Beckman, 591–602
- Hlavacek-Larrondo, J., Gendron-Marsolais, M. L., Fecteau-Beaucage, D., et al. 2018, *MNRAS*, 475, 2743
- Hoang, D. N., Shimwell, T. W., van Weeren, R. J., et al. 2018, *MNRAS*, 478, 2218
- Hoang, D. N., Shimwell, T. W., van Weeren, R. J., et al. 2019, *A&A*, 622, A21
- Hoang, D. N., Zhang, X., Stuardi, C., et al. 2021, *A&A*, 656, A154
- Hoefl, M. & Brüggen, M. 2007, *MNRAS*, 375, 77
- Hoefl, M., Rajpurohit, K., Wittor, D., di Gennaro, G., & Domínguez-Fernández, P. 2022, *arXiv e-prints*, arXiv:2201.03208
- Hong, S. E., Kang, H., & Ryu, D. 2015, *ApJ*, 812, 49
- Hutschenreuter, S., Anderson, C. S., Betti, S., et al. 2021, *arXiv e-prints*, arXiv:2102.01709
- Iapichino, L. & Brüggen, M. 2012, *MNRAS*, 423, 2781
- Inchingolo, G., Wittor, D., Rajpurohit, K., & Vazza, F. 2022, *MNRAS*, 509, 1160
- Johnston-Hollitt, M. & Ekers, R. D. 2004, *arXiv e-prints*, astro
- Jonas, J. & MeerKAT Team. 2016, in *MeerKAT Science: On the Pathway to the SKA*, 1
- Jones, A., de Gasperin, F., Cuciti, V., et al. 2021, *MNRAS*, 505, 4762
- Jones, F. C. & Ellison, D. C. 1991, *Space Sci. Rev.*, 58, 259
- Kale, R., Dwarakanath, K. S., Bagchi, J., & Paul, S. 2012, *MNRAS*, 426, 1204
- Kale, R., Wik, D. R., Giacintucci, S., et al. 2017, *MNRAS*, 472, 940
- Kang, H. 2015, *Journal of Korean Astronomical Society*, 48, 155
- Kang, H. & Ryu, D. 2016, *ApJ*, 823, 13
- Knowles, K., Cotton, W. D., Rudnick, L., et al. 2022, *A&A*, 657, A56
- Lee, W., James Jee, M., Finner, K., et al. 2022, *ApJ*, 924, 18
- Lindner, R. R., Baker, A. J., Hughes, J. P., et al. 2014, *ApJ*, 786, 49
- Loi, F., Murgia, M., Vacca, V., et al. 2020, *MNRAS*, 498, 1628
- Offringa, A. R., McKinley, B., Hurley-Walker, et al. 2014, *MNRAS*, 444, 606
- Offringa, A. R. & Smirnov, O. 2017, *MNRAS*, 471, 301
- Ogrean, G. A., Brüggen, M., van Weeren, R. J., Burgmeier, A., & Simionescu, A. 2014, *MNRAS*, 443, 2463
- Owen, F. N., Rudnick, L., Eilek, J., et al. 2014, *ApJ*, 794, 24
- Parekh, V., Kincaid, R., Thorat, K., et al. 2022, *MNRAS*, 509, 3086
- Perley, R. A. & Butler, B. J. 2013, *The Astrophysical Journal Supplement Series*, 206, 16
- Pinzke, A., Oh, S. P., & Pfrommer, C. 2013, *MNRAS*, 435, 1061
- Pizzo, R. F., de Bruyn, A. G., Bernardi, G., & Brentjens, M. A. 2011, *A&A*, 525, A104
- Planck Collaboration, Ade, P. A. R., Aghanim, N., et al. 2016, *A&A*, 594, A27
- Rajpurohit, K., Hoefl, M., van Weeren, R. J., et al. 2018, *ApJ*, 852, 65
- Rajpurohit, K., Hoefl, M., Vazza, F., et al. 2020, *A&A*, 636, A30
- Rajpurohit, K., Hoefl, M., Wittor, D., et al. 2022a, *A&A*, 657, A2
- Rajpurohit, K., van Weeren, R. J., Hoefl, M., et al. 2022b, *ApJ*, 927, 80
- Randall, S. W., Clarke, T. E., van Weeren, R. J., et al. 2016, *ApJ*, 823, 94
- Rau, U. & Cornwell, T. J. 2011, *A&A*, 532, A71
- Rengelink, R. B., Tang, Y., de Bruyn, A. G., et al. 1997, *A&AS*, 124, 259
- Riseley, C. J., Scaife, A. M. M., Wise, M. W., & Clarke, A. O. 2017, *A&A*, 597, A96
- Roettiger, K., Burns, J. O., & Stone, J. M. 1999, *ApJ*, 518, 603
- Schnitzeler, D. H. F. M. & Lee, K. J. 2017, *MNRAS*, 466, 378
- Skillman, S. W., Xu, H., Hallman, E. J., et al. 2013, *ApJ*, 765, 21
- Struble, M. F. & Rood, H. J. 1999, *ApJS*, 125, 35
- Stuardi, C., Bonafede, A., Lovisari, L., et al. 2021, *MNRAS*, 502, 2518
- Stuardi, C., Bonafede, A., Wittor, D., et al. 2019, *MNRAS*, 489, 3905
- Urdampilleta, I., Simionescu, A., Kaastra, J. S., et al. 2021, *A&A*, 646, A95
- van Haarlem, M. P., Wise, M. W., Gunst, A. W., et al. 2013, *A&A*, 556, A2
- van Weeren, R. J., Bonafede, A., Ebeling, H., et al. 2012, *MNRAS*, 425, L36
- van Weeren, R. J., Brüggen, M., Röttgering, H. J. A., et al. 2011a, *A&A*, 533, A35
- van Weeren, R. J., de Gasperin, F., Akamatsu, H., et al. 2019, *Space Sci. Rev.*, 215, 16
- van Weeren, R. J., Hoefl, M., Röttgering, H. J. A., et al. 2011b, *A&A*, 528, A38
- van Weeren, R. J., Röttgering, H. J. A., Bagchi, J., et al. 2009, *A&A*, 506, 1083
- Vazza, F. & Brüggen, M. 2014, *MNRAS*, 437, 2291
- Vazza, F., Brüggen, M., Wittor, D., et al. 2016, *MNRAS*, 459, 70
- Vazza, F., Brunetti, G., Brüggen, M., & Bonafede, A. 2018, *MNRAS*, 474, 1672
- White, J. A., Canning, R. E. A., King, L. J., et al. 2015, *MNRAS*, 453, 2718
- Wittor, D., Etori, S., Vazza, F., et al. 2021, *MNRAS*, 506, 396
- Wittor, D., Hoefl, M., Vazza, F., Brüggen, M., & Domínguez-Fernández, P. 2019, *MNRAS*, 490, 3987
- Wittor, D., Vazza, F., Ryu, D., & Kang, H. 2020, *MNRAS*, 495, L112
- Zhang, C., Churazov, E., Forman, W. R., & Lyskova, N. 2019, *MNRAS*, 488, 5259
- Zhang, X., Simionescu, A., Kaastra, J. S., et al. 2020, *A&A*, 642, L3
- Zhang, X., Simionescu, A., Stuardi, C., et al. 2021, *A&A*, 656, A59
- Zheng, Q., Johnston-Hollitt, M., Duchesne, S. W., & Li, W. T. 2018, *MNRAS*, 479, 730

**Table A.1.** Broad-band spectrum for PSZ1 G096.89+24.17. Column 1: radio relic; Column 2: frequency; Column 3: flux density with  $1\sigma$  uncertainty; Column 4: spectral index derived from power-law fitting with associated uncertainty.

Relic	$\nu$ [MHz]	$S_\nu$ [mJy]	$\alpha$
North	140	$76 \pm 12$	$0.92 \pm 0.04$
	380	$27 \pm 3$	
	610	$17 \pm 2$	
	1500	$7.8 \pm 0.4$	
South	140	$276 \pm 42$	$1.14 \pm 0.03$
	380	$74 \pm 7$	
	610	$46 \pm 5$	
	1500	$16.5 \pm 0.9$	

**Table A.2.** Broad-band spectrum for El Gordo. Column 1: radio relic; Column 2: frequency; Column 3: flux density with  $1\sigma$  uncertainty; Column 4: spectral index derived from power-law fitting with associated uncertainty.

Relic	$\nu$ [MHz]	$S_\nu$ [mJy]	$\alpha$
North West	325	$44 \pm 4$	$1.25 \pm 0.04$
	610	$21 \pm 2$	
	2100	$4.3 \pm 0.2$	
East	325	$2.9 \pm 0.3$	$1.06 \pm 0.04$
	610	$1.4 \pm 0.1$	
	2100	$0.41 \pm 0.04$	

**Table A.3.** Broad-band spectrum for ZwCl 2341.1+0000. Column 1: radio relic; Column 2: frequency; Column 3: flux density with  $1\sigma$  uncertainty; Column 4: spectral index derived from power-law fitting with associated uncertainty.

Relic	$\nu$ [MHz]	$S_\nu$ [mJy]	$\alpha$
North	144	$40 \pm 4$	$1.02 \pm 0.02$
	1500	$3.7 \pm 0.2$	
	3000	$1.7 \pm 0.1$	
South	144	$126 \pm 13$	$0.98 \pm 0.02$
	1500	$12.2 \pm 0.7$	
	3000	$6.4 \pm 0.3$	

## Appendix A: Broad-band integrated radio spectra

In order to reduce the uncertainties on the Mach number estimates used in Sec. 4.2, we required that all radio relics with polarization information have spectral index estimates with uncertainties lower than 0.1. For this reason, we computed the broad-band integrated spectral index of three double radio relics, namely PSZ1 G096.89+24.17 (a.k.a. ZwCl 1856.8+6616), El Gordo, and ZwCl 2341.1+0000. We used both archival and proprietary data from which we derived flux density measurements. The uncertainty on the flux density were computed taking into account both statistical noise and calibration errors:

$$\sigma_S = \sqrt{(\delta S \times S)^2 + (\sigma \times \sqrt{n_{\text{beam}}})^2}, \quad (\text{A.1})$$

where the calibration error,  $\delta$ , is 5 % for JVL A and 10 % for GMRT and LOFAR observations,  $\sigma$  is the rms noise of the image, and  $n_{\text{beam}}$  is the number of resolution elements contained in the region used to measure the flux density. We then computed the spectral index and its uncertainty with a standard power-law fitting.

For PSZ1 G096.89+24.17, we used flux density measurements at 140 MHz and 1.5 GHz from Jones et al. (2021) and we computed 380 and 610 MHz flux densities from proprietary GMRT observations (Rajpurohit et al. in preparation). For El Gordo we measured the flux density at 325 and 610 MHz using archival observations (observed during 2017), and we used the 2.1 GHz measurement from Lindner et al. (2014). For ZwCl2341 we used the 1.5 GHz images published in this work, 3 GHz measurements from Benson et al. (2017) and 144 MHz flux densities from proprietary LOFAR data (Hoang et al. in preparation). Flux density measurements and resulting integrated spectral index are listed in Tab. A.1, Tab. A.2, and Tab. A.3 for PSZ1 G096.89+24.17, El Gordo, and ZwCl 2341.1+0000, respectively. Power-law fits are displayed in Fig. A.1.

We notice that for three clusters (namely, Abell 3365, El Gordo and RXC J1314.4-2515) we attempted a spectral fitting using the enhanced imaging products released by the MeerKAT Galaxy Cluster Legacy Survey (Knowles et al. 2022). However, we found that the flux densities measured from these survey were inconsistent with other measurements, leading to unreliable steep spectral indexes ( $> 2$ ). Hence, we did not include MeerKAT data here.



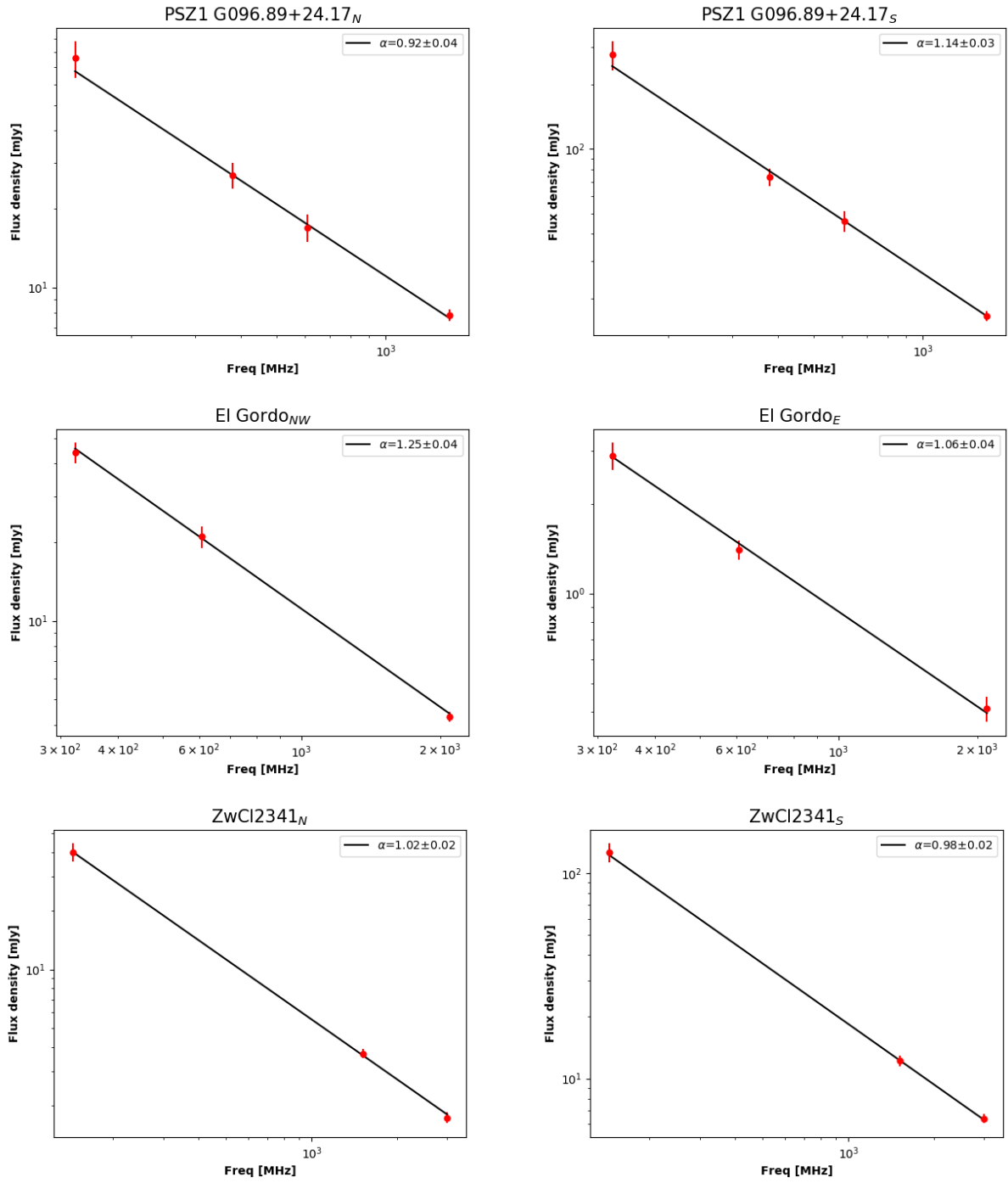


**Fig. A.1.** Power-law fit to the flux density measurements listed in Tab. A.1, Tab. A.2 and Tab. A.3